

REPORT DOCUMENTATION PAGE

Form Approved
OMB NO. 0704-0188

Public Reporting burden for this collection of information is estimated to average 1 hour per response, including the time for reviewing instructions, searching existing data sources, gathering and maintaining the data needed, and completing and reviewing the collection of information. Send comment regarding this burden estimates or any other aspect of this collection of information, including suggestions for reducing this burden, to Washington Headquarters Services, Directorate for Information Operations and Reports, 1215 Jefferson Davis Highway, Suite 1204, Arlington, VA 22202-4302, and to the Office of Management and Budget, Paperwork Reduction Project (0704-0188), Washington, DC 20503.

1. AGENCY USE ONLY (Leave Blank)		2. REPORT DATE 20 March 98	3. REPORT TYPE AND DATES COVERED Final
4. TITLE AND SUBTITLE Concept Study of Multi Sensor Detection Imaging and Explosive Confirmation of Mines		5. FUNDING NUMBERS 2172040 76A-7270 P665502 86100-2581S31124 7X00ST/7ST37478	
6. AUTHOR(S) Larry G. Stolarczyk		8. PERFORMING ORGANIZATION REPORT NUMBER Final - #6	
7. PERFORMING ORGANIZATION NAME(S) AND ADDRESS(ES) Raton Technology Research, Inc. 848 Clayton Highway Raton, NM 87740		9. SPONSORING / MONITORING AGENCY NAME(S) AND ADDRESS(ES) U. S. Army Research Office P.O. Box 12211 Research Triangle Park, NC 27709-2211	
10. SPONSORING / MONITORING AGENCY REPORT NUMBER G3 ARO 37478.1-PH-5T /		11. SUPPLEMENTARY NOTES The views, opinions and/or findings contained in this report are those of the author(s) and should not be construed as an official Department of the Army position, policy or decision, unless so designated by the documentation.	
12 a. DISTRIBUTION / AVAILABILITY STATEMENT Approved for public release; distribution unlimited.		12 b. DISTRIBUTION CODE	
13. ABSTRACT (Maximum 200 words) To achieve a quantum leap forward in humanitarian demining and counter mining, a handheld instrument capable of detecting metallic and non-metallic landmines is needed. Metal detectors (MD) cannot detect non-metallic mines and detection sensitivity degrades in magnetic soil. Because metal detection sensitivity can be increased to detect low metal content in some non-metallic mines, some alarms significantly increase. Prodding the soil overlying a suspected mine with metal rods is needed to create a mental image of the object. Imaging, especially high resolution imaging, would minimize and perhaps eliminate prodding. This scientific and engineering study concluded that electromagnetic wave detection and imaging technology (EDIT) featuring a resonant microstrip patch antenna (RMPA) provides a quick-look at shallow buried objects. Scans of 1X1 meter square areas can be completed in minutes while producing silhouettes of the buried objects. Lateral migration radiography (LMR) and nuclear quadripole resonance (NQR) instruments become field deployable when only required to scan the area of the EDIT silhouette. Much higher resolution of LMR contributes to the quantum leap forward in landmine detection technology.			
14. SUBJECT TERMS Landmine detection and imaging, anti-personnel landmine detection and imaging, non-metallic landmine detection and imaging, lateral migration radiography (LMR), nuclear quadrupole resonance (NQR) demining system.		15. NUMBER OF PAGES 64	
16. PRICE CODE			
17. SECURITY CLASSIFICATION OR REPORT UNCLASSIFIED	18. SECURITY CLASSIFICATION ON THIS PAGE UNCLASSIFIED	19. SECURITY CLASSIFICATION OF ABSTRACT UNCLASSIFIED	20. LIMITATION OF ABSTRACT UL

NSN 7540-01-280-5500

Standard Form 298 (Rev. 2-89)

Prescribed by ANSI Std. Z39-18

298-102

DTIC QUALITY INSPECTED 2

Enclosure 1

11
" Best Available Copy



RATON TECHNOLOGY RESEARCH

848 Clayton Road • P.O. Box 428 • Raton, NM 87740
Telephone: (505) 445-3607 • FAX: (505) 445-9659

INVOICE

U.S. Army Research Office
Attn: Amy Wendelgass
Contracting Officer
4300 S. Miami Blvd.
P.O. Box 12211
Research Triangle Park, NC 27709-2211

DATE: March 20, 1998

INVOICE NO.: 398-01

TERMS: Per Contract

CONTRACT #: DAAG55-97-C-0057

Final technical report "Multi Sensor Detection Imaging and Explosive Confirmation of Mines" per referenced contract.

Final Report \$16,670.00

TOTAL INVOICE \$16,670.00

Contract Number DAAG55-97-C-0057

**Small Business
Technology Transfer (STTR)
Solicitation Topic 97T006**

**Multi-Sensor Detection, Imaging, and
Explosive Confirmation of Mines**

Final Report

For Period Ending 20 January 1998

**US Army Research Office
Attn: AMXRO-ICA, P.O. Box 12211
Research Triangle Park, NC 27709-2211**

Prepared for

**Dr. Jack Rowe
US Army Research Office
4300 S. Miami Blvd., P.O. Box 12211
Research Triangle Park, NC 27709-2211**

Prepared by

**Raton Technology Research, Inc.
848 Clayton Highway
Raton, New Mexico 87740**

19980519 026



Table of Contents

Overview	1
1. LATERAL MIGRATION RADIOGRAPHY	2
1.1 LMR Principles.....	2
1.1.2 LMR Instrumentation	2
1.1.2 General Results	3
1.2 LANDMINE SIGNATURES	4
1.2.1 Air Volume	4
1.2.2 Lateral Migration Shifting	5
1.2.3 Shadowing Effect.....	7
2. PROPOSED LMR SYSTEM DESIGN	10
2.1 General Configuration.....	10
2.1.1 LMR Vehicle Configuration	10
2.1.2 Definition of Motion.....	11
2.2 X-ray Generators	13
2.2.1. LORAD X-ray Generators	13
2.2.2. Aerosino AX160-2-15	17
2.3 Rotating Collimator	17
2.3.1. Configuration	17
2.3.2. Pixel Pattern and Diameter of Rotating Collimator.....	19
2.3.3. Angular Speed of the Rotating Collimator.....	21
2.3.4. Self-normalization of Pixel Dwell Time	21
2.3.5. MCNP simulation	22
2.4 Detector Design and Optimization	25
2.4.1 Multiple Miniature Photomultiplier Tubes Case	25
2.4.2 Single Photomultiplier Tube with Light Pipe Case	26
2.5 Image Acquisition and Processing.....	26
2.5.1 Color Coding and Image Acquisition.....	26
2.5.2 Image Segmentation and Labeling	27
2.5.3. Image Correlation Processing.....	27
2.5.4 Mine Identification.....	31
3. Resonant Microstrip Patch Antenna	33
3.1 RMPA Principles.....	33
3.2 Land Mine Detection.....	35
3.2.1. RMPA Detection Sensitivity	36
3.2.2. RMPA Antenna Development.....	38



Table of Contents (concluded)

4. EDIT Land Mine Detector	40
4.1 EDIT System Description.....	40
4.1.1. Sensor Head.....	40
4.1.2. User Interface	41
4.1.3. Power Management.....	43
4.2 EDIT Mechanical and Software Design	45
4.2.1. Prototype Assembly.....	45
4.2.2. Chassis and Cable System.....	46
4.2.3 System Software.....	48
5. Positioning Systems	49
5.1 RF X-Y Positioning System.....	49
5.1.1 Description of EDIT Detector X-Y Positioning System.....	49
5.1.2 Positioning System Instrumentation.....	51
5.2 Sonic X-Y Positioning System	51
6. Nuclear Quadripole Resonance (NQR)	53
7. SYSTEM RELATIONSHIP.....	54
7.1 System Integration.....	54
8. Appendix	55

Figures

1. Schematic of measurement setup used for the LMR landmine detection simulations ..	2
2. VS-1.6 antipersonnel mine, 1 inch depth-of-burial, 15 mm resolution.....	5
3. M19 antitank mine, 1 inch depth-of-burial, 15 mm resolution.....	6
4. TMA-4 mine LMR image with 1 inch resolution.....	7
5. TS/50 antipersonnel mine, on surface, 15 mm resolution.....	9
6. TS/50 antipersonnel mine, flush DOB, 15 mm resolution.....	10
7. Concept diagram of LMR land mine detection vehicle.....	11
8. X-ray beam trace on soil surface.....	12
9. Lorad LPX-160 x-ray generator tube head and liquid cooling unit.....	14
10. Lorad LPX-160 x-ray generator air-cooled tube head and digital control unit.....	15
11. Diagram of 6 inches diameter plastic disk with four holes (diameters in inches)	16
12. Plastic disk images obtained with Lorad LPX-160 (left) and Maxitron 300 (right).....	16
13. Side view of the rotating collimator.....	18
14. Cross section view of the rotating collimator.....	19
15. Extended view of inner and outer cylinders of the rotating collimator.....	19



16. X-ray beam illumination pattern on the soil surface with rotating collimator.....	20
17. The rotating collimator diameter calculation diagram.	21
18. Dwell time calculation diagram.	22
19. Illustration of raster direction distortion in LMR images by x-ray beam angle tilting....	23
20. MCNP simulated images of a solid mine off-center of the image.	24
21. MCNP simulated images (uncollimated) with mine at the center of the images.	25
22. Mean filter mask.	27
23. Surface features removal illustration.	28
24. LMR images of a plastic mine buried with slope surface.	29
25. LMR images of a pothole.....	30
26. Vertical cross section of the RMPA sensor including electric field lines.....	33
27. Measured 850 MHz RMPA sensor feedpoint impedance versus frequency.....	34
28. Frequency comparison of RMPA impedance response to a plastic mine at 5 cm depth in 1% moisture sand.	37
29. RMPA impedance response to a soil void and surface mound using the 821/616 MHz frequency, 10.2 di-electric dual feed-point patch.....	39
30. Photographs of the EDIT Land Mine Detector Sensor Head built for prototype testing of the hand-held unit.	41
31. Photograph of the newly operational Seiko G321EX display screen.....	42
32. Diagrams of the user interface display showing the potential order of operation. This procedure will include system tests, sensor calibration, home positioning, and finally the recording of field measurements.	43
33. Advanced Power Center containing microcomputer controlled battery monitoring circuitry, charging jacks, 9-pin serial port, power warning speaker, and external fuse jack.	44
34. Block diagram of EDIT Land Mine Detector sub-systems.....	45
35. Series of photos showing the deployment procedure for the EDIT detector.....	46
36. Schematic of EDIT wire harness and connector design and module conductor assignments.	47
37. Configuration of Receiver Antenna Base Line with 10 meter Separation during field survey.....	49
38. Block Diagram of X-Y Positioning System's phase sensitive electronics.....	50

Tables

Table 1. Motion speed and image interrogation time for x-ray generator power at 100 W and 15 mm resolution.	13
Table 2. Lorad LPX-160 liquid cooled unit physical parameters.....	13
Table 3. Lorad LPX-160 air-cooled unit physical parameters.....	14



Overview

Lateral migration radiography (LMP) is a new Compton backscatter imaging modality. LMR can detect both metallic mines and plastic mines up to 10 cm depth-of-burial. The mines show up clearly in the images with vivid signatures that depend upon (for plastic mine) the mine air volumes and the geometric shape. The LMR landmine detection system will use an off-the-shelf x-ray generator with high-efficiency detectors. The raster direction scanning of the x-ray source will be achieved by a rotating collimator cover over the x-ray tube head. The forward motion of the LMR system to the suspected area, color-marked by the RMPA system, will be controlled by the RF or sonic x-y positioning system which is also used by the RMPA system. This locating system also is used to control the motion axis during LMR image acquisition. The LMR system will use state-of-the-art data acquisition techniques to achieve quick, low noise mine images. Image processing and pattern recognition algorithms should essentially eliminate both false negatives and false positives and provide mine type identification.

The EDIT Land Mine Detector Sensor Head has been assembled with the operational antenna and electronics being built by RTR personnel. The RMPA electronics assembly, connected via PC-104 bus, and the LANL positioning subsystem are mounted within the head. The chassis shaft assemblies are composed of aluminum 3-section telescopic tubes that allow user height adjustment. The shafts contain pigtail cables within their inner diameter, which travel from the display to the sensor head and battery center. The battery enclosures consist of two aluminum tubes mounted to the base of the rear shaft, each with the capacity to hold 4 D-cell batteries inserted into the rear of the tubes similar to a flashlight. A power management circuit monitors battery life and supplies all the real time battery data. The assembled detector prototype, with patch antenna, graphical user interface, and 8 D-cell batteries installed weighs just over 18 lbs. The deliverable version of the x-y positioning system is lighter and more robust. The GUI display processor has been upgraded to an Elan SC410 microprocessor chip to be used with an external video controller allowing higher grayscale resolution. In addition, several menus have been developed for the display using the QNX operating system graphical user interface language Photon. The measurement capabilities of the EDIT electronics is now being explored and data should be available by mid-April. The control software for the measurement instrumentation has been completed and tested with the new Power/Input/Output Interface board. The deliverable version of the x-y positioning system is currently being built by LANL. The RF modems are now able to communicate xy data. A proposed field test plan for local outdoor EDIT experiments should provide verification of successful sub-system integration and reveal areas of unit operation requiring further development. Work is still underway to adapt the detection algorithm to the specific characteristics of the hardware and adapt the system to the wide range of field conditions anticipated.

Further collaboration with Dr. Al Garroway of the Naval Research Laboratory on issues of explosives coverage with NQR is pending. Experts are currently assessing the direct combination of the associated hardware of RMPA and NQR

1. LATERAL MIGRATION RADIOGRAPHY

1.1 LMR Principles

1.1.2 LMR Instrumentation

The LMR system includes an x-ray generator with articulating collimator, two sets of detectors, a computer with a data acquisition board and display and an electric power generator mounted on a suitable platform vehicle. The detectors include two collimated detectors and two uncollimated detectors (see Figure 1.). The two uncollimated detectors primarily register first-collision photons which carry substantially surface feature information. The two collimated detectors predominately register multiple-collision photons which carry surface feature and subsurface feature information. This functionality is achieved by optimizing the sets of collimators. These two sets of detectors are set up symmetrically (fore and aft relative to the x-ray illumination beam) with the two uncollimated detectors separated by a gap for the x-ray illumination beam and the two collimated detectors adjacent (and outboard relative) to the two uncollimated detectors.

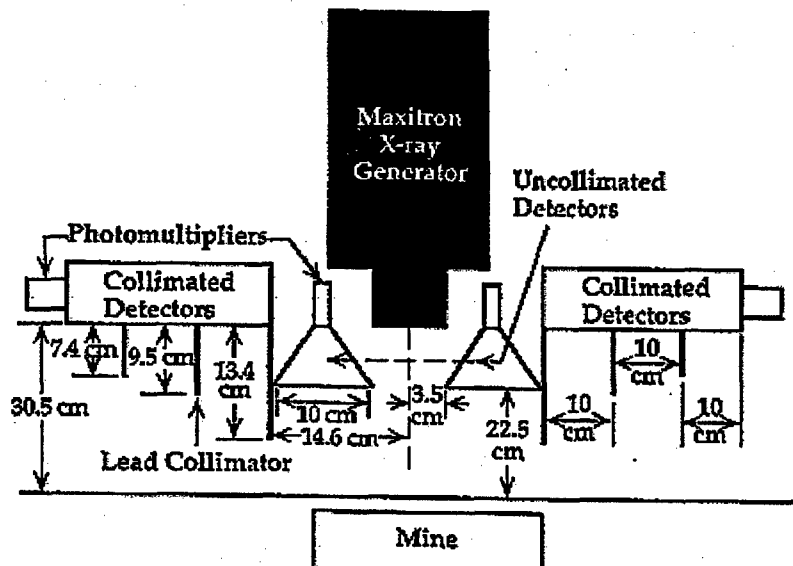


Figure 1. Schematic of measurement setup used for the LMR landmine detection simulations.



For the x-ray energies of interest in the LMR system (130 to 180 kVp x-ray spectra with mean x-ray energies of around 40 to 60 keV) two kinds of significant interactions exist: 1. The photoelectric effect. Compton scatter. In the photoelectric effect, the photon is absorbed and an electron is emitted. In Compton scatter, the photon is inelastically scattered and there is energy transferred from the photon to the electron. These two interactions are a function of the effective atomic number (Z) and electron density of the material and they form the basis of the land mine detection process. Since air (due to fuse well and blast directing volume in a mine), soil, plastics, metals and explosives have different Z numbers and different electron densities, they show intensity contrast in LMR images. Soil is the ambient background in land mine detection and is compared to the properties of other material and structures. A plastic mine has a lower Z number while metal used in land mines has a higher atomic number than that of soil. In the case of air, the Z number is higher, but the electron density is substantially lower than that of the soil. For an x-ray photon energy of about 50 keV or lower, the higher Z materials have higher photoelectric effect cross section and a lower Compton scatter cross section. For low Z materials it is just the opposite. Air has a lower cross section for both the photoelectric effect and Compton scatter than soil because of its low density.

1.1.2 General Results

In LMR images, materials such as metals with a higher photoelectric effect cross section than that of soil show intensity decreases in the images. In contrast, materials such as plastic mines, wood, etc. with a lower photoelectric effect cross section and a higher Compton scatter cross section than those of soil show intensity increases in the images.

As multiple-collision photons laterally migrate through the soil, structured electron density variations in the soil are registered. These photons, predominately detected by the collimated detector, show the discontinuities of different objects in the soil. Therefore, the collimated detector images show the contrast of the transport media traversed by the photons.

Because of the photon lateral migration in the media, there is lateral migration shifting in both of the collimated detector images. The image shift direction in the front detector image is backward and, for the same reason, forward in the rear detector. This shift increases with mine depth-of-burial and is thereby a measure of the burial depth.

Because the collimated detector registers both surface and subsurface features and the uncollimated detector predominately registers surface features, surface feature removal can be achieved in LMR images.



1.2 LANDMINE SIGNATURES

1.2.1 Air Volume

In LMR images, the inner air volume shapes combined with the outer geometric shapes of the land mines yield key signature features for land mine detection and identification. For detonator operation, every land mine has at least one fuse well to accommodate the fuse, detonator and booster. This fuse well, essentially an air volume with some plastics or metals, shows up clearly and uniquely in the LMR images.

Basically, air gives free flight to the photons. The existence of air volumes in real mines dramatically modifies the once-scattered photon exit path as well as the multiple-scattered photon migration path, when compared to simulated mines that lack these air spaces. When the x-ray beam is directly scanning over the air volumes, the photons which can pass through the mine casing material without any interaction will interact with the bottom or side wall of the fuse well. The solid angles subtended by the LMR detectors to these photons are smaller than those of the photons interacting with a simulated mine without air volume. For all the photons at the first-collision sites, the probability of not being registered by the uncollimated detectors is higher than that of the simulated mine case. As a consequence, an intensity decrease occurs at the location of the center of the air volume in the uncollimated detector images (Figure 2 and 3.).

When the x-ray beam is scanning right at the edge of the air volumes, photons emitted in the direction of the air volume will have a higher probability of being registered by the uncollimated detectors than the photons emitted in the direction of the mine material. Therefore, there are high intensity areas right at the edge of the air volume and they occur at the front and back edge of the air volume in the rear and front uncollimated detector images respectively (see Figure 2 and 3.).

For multiple-scattered photons, the physical existence of the air volume modifies the photon field in the transport media. But because the air volume essentially gives free flight to the migrating photons and the multiple scattering of photons tends to average out the effect of the air volume, there is a diffused evidence of the air volume in the collimated detector images. Therefore, in Figure 2, the collimated detector images do not show air volumes with the singular definition shown in the uncollimated detector acquired images.



RATON
TECHNOLOGY
RESEARCH

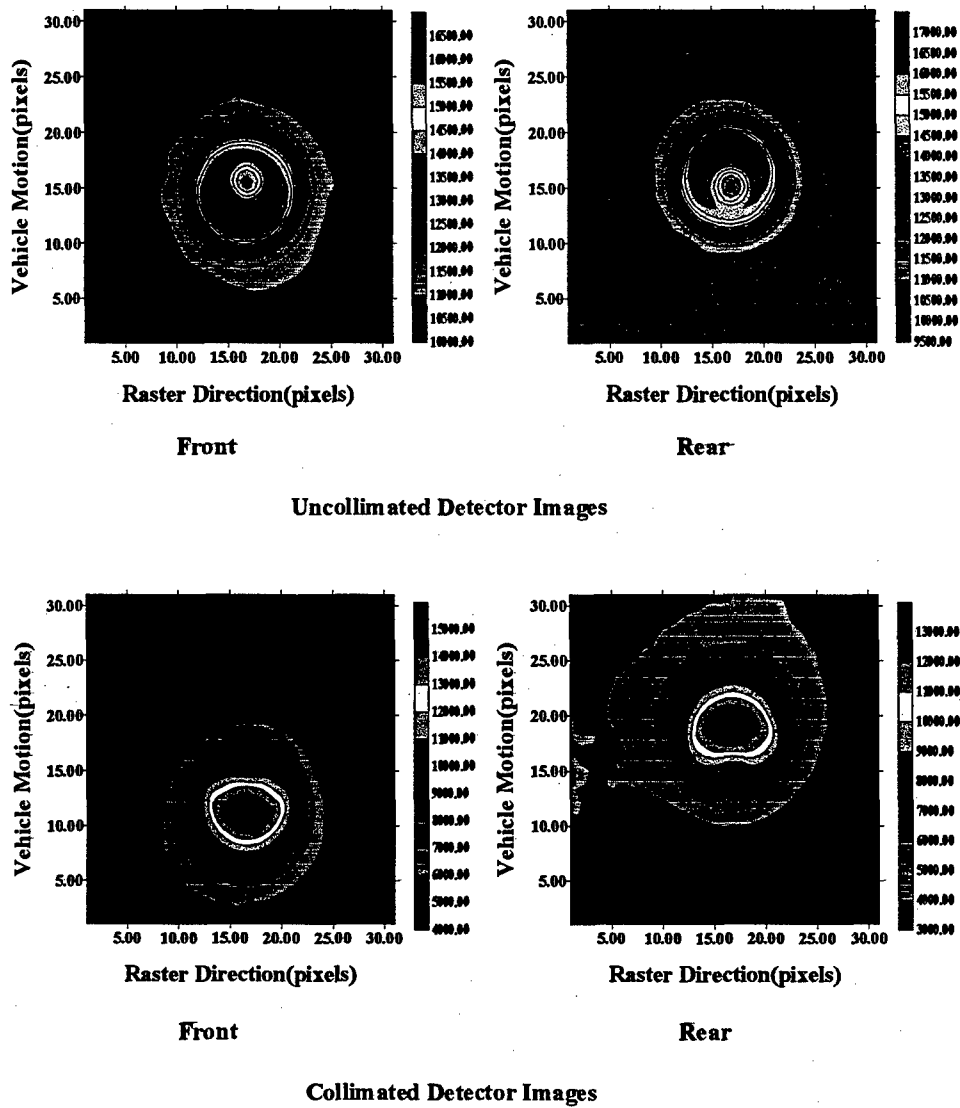


Figure 2. VS-1.6 antipersonnel mine, 1 inch depth-of-burial, 15 mm resolution.

1.2.2 Lateral Migration Shifting

Monte Carlo numerical simulations and experiments have demonstrated the different ways in which the uncollimated and the collimated detectors function in an LMR system and form the bases of the physical phenomena discussion in the previous sections as well as the discussion



of origin of LMR image contrast. Photon lateral migration is very prominent in the collimated detector images. In the collimated images of Figure 3., vehicle motion-direction shifting exists in both the front and rear detector images and their shifts are opposite. For a plastic mine with the Compton scatter cross section greater than that of the soil, the number of multiple-scattered photons detected is greater than that from the soil and this causes the intensity increase in the images. Among the multiple-scattered photons, those migrating through the mine have a higher probability of being registered by detectors. Therefore, during x-ray beam scanning, as the mine is initially encountered, the front collimated detector registers a higher intensity than the rear collimated detector. Similarly, when x-ray scanning is on the final encountered mine edge, the rear detector registers more Compton scatter photons than the front detector.

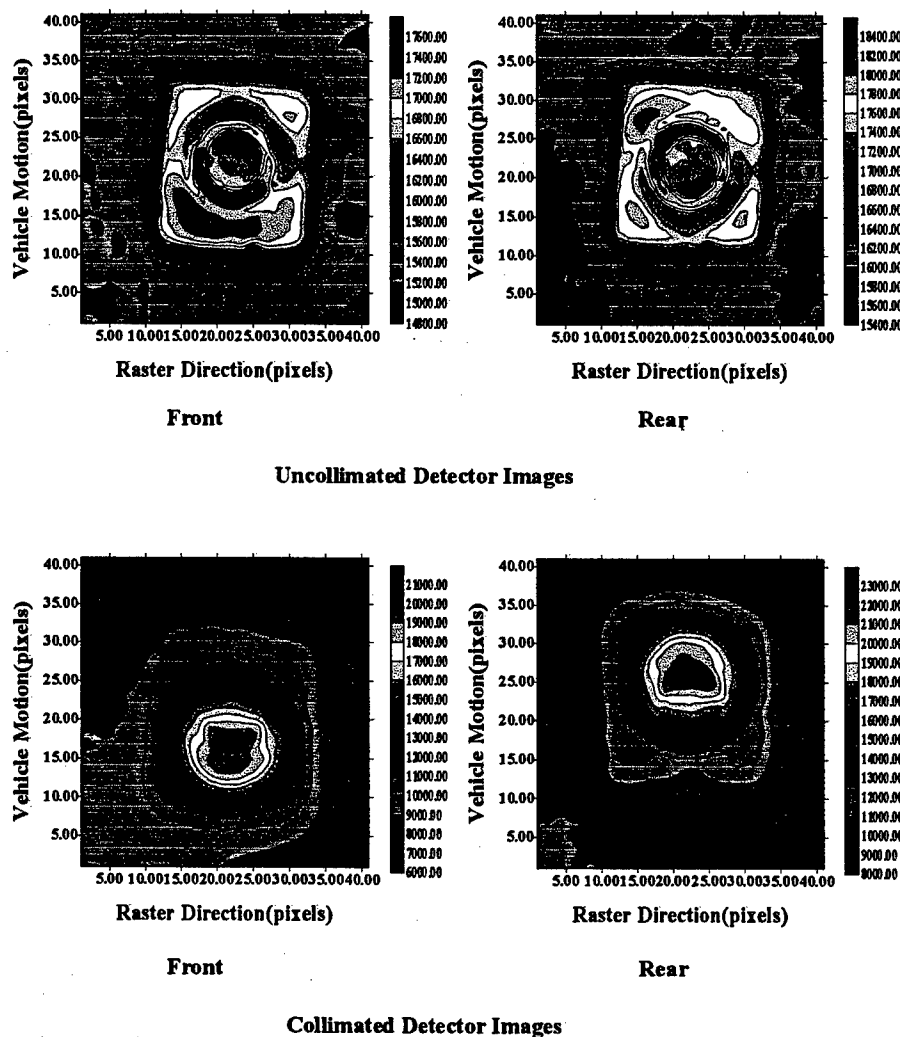
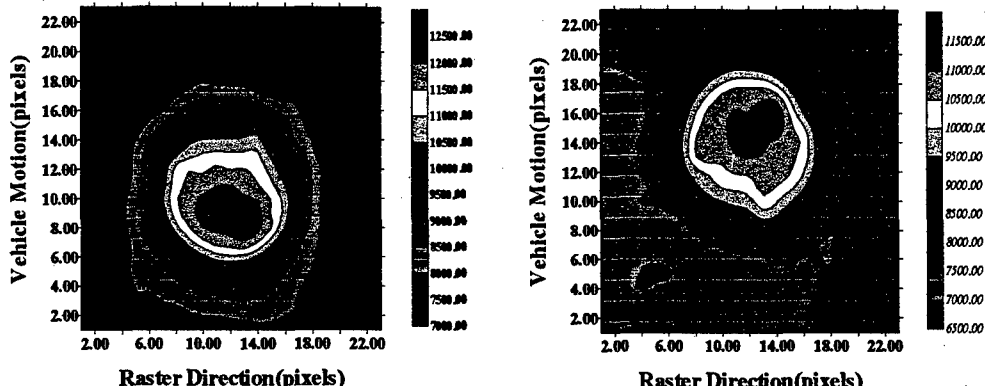


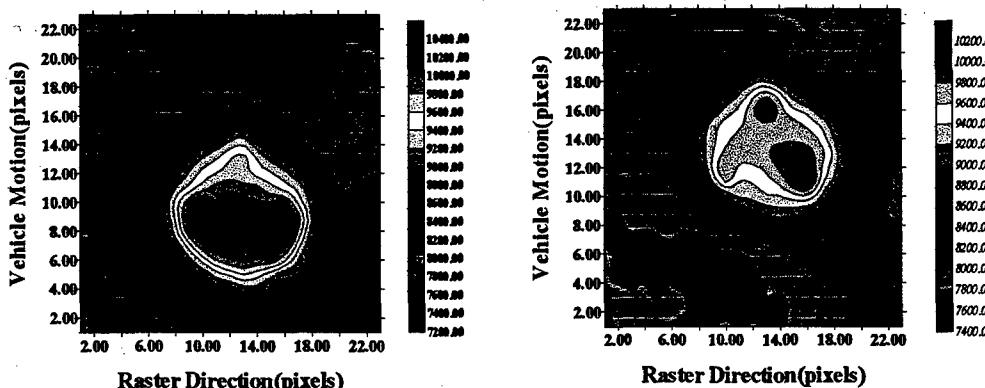
Figure 3. M19 antitank mine, 1 inch depth-of-burial, 15 mm resolution.



Due to this behavior, the highest intensity in the front collimated detector image tends to show up earlier than the physical center of the mine, which appears as backward shifting. In the rear collimated detector image the opposite happens. This shifting is proportional to the depth-of-burial of the land mine; therefore, the depth-of-burial of the mine can be estimated from the amount of shifting (see Figure 4.).



Collimated Images (1 inch DOB)



Collimated Images (2 inch DOB)

Figure 4. TMA-4 mine LMR image with 1 inch resolution.

1.2.3 Shadowing Effect

There are also various shadowing effects in the LMR images, especially if the mine is laid on the soil surface. In Figure 5., the shadows clearly accompany the mine images of both the collimated and uncollimated detectors. The shadows are roughly symmetric about the raster direction axis as shown in both the uncollimated images and collimated images. In contrast,



there is no shadowing effect in the images of Figure 6. Shadowing effects are the result of the surface laid mine physically blocking some of the Compton scatter photons. As the x-ray beam scans toward the mine, some of the Compton scatter photons emitted from the soil cannot reach the front detectors because of blocking by the land mine. Similarly, as the x-ray beam moves away from the mine, some of the Compton photons are blocked so they cannot be registered by the rear detectors. Therefore, the shadows are behind the mine in the front detector images and in front of the mine in the rear detector images. In actual deployment, antipersonnel mines are usually put either on the soil surface or they have a shallow depth-of-burial, normally not more than a few centimeters.

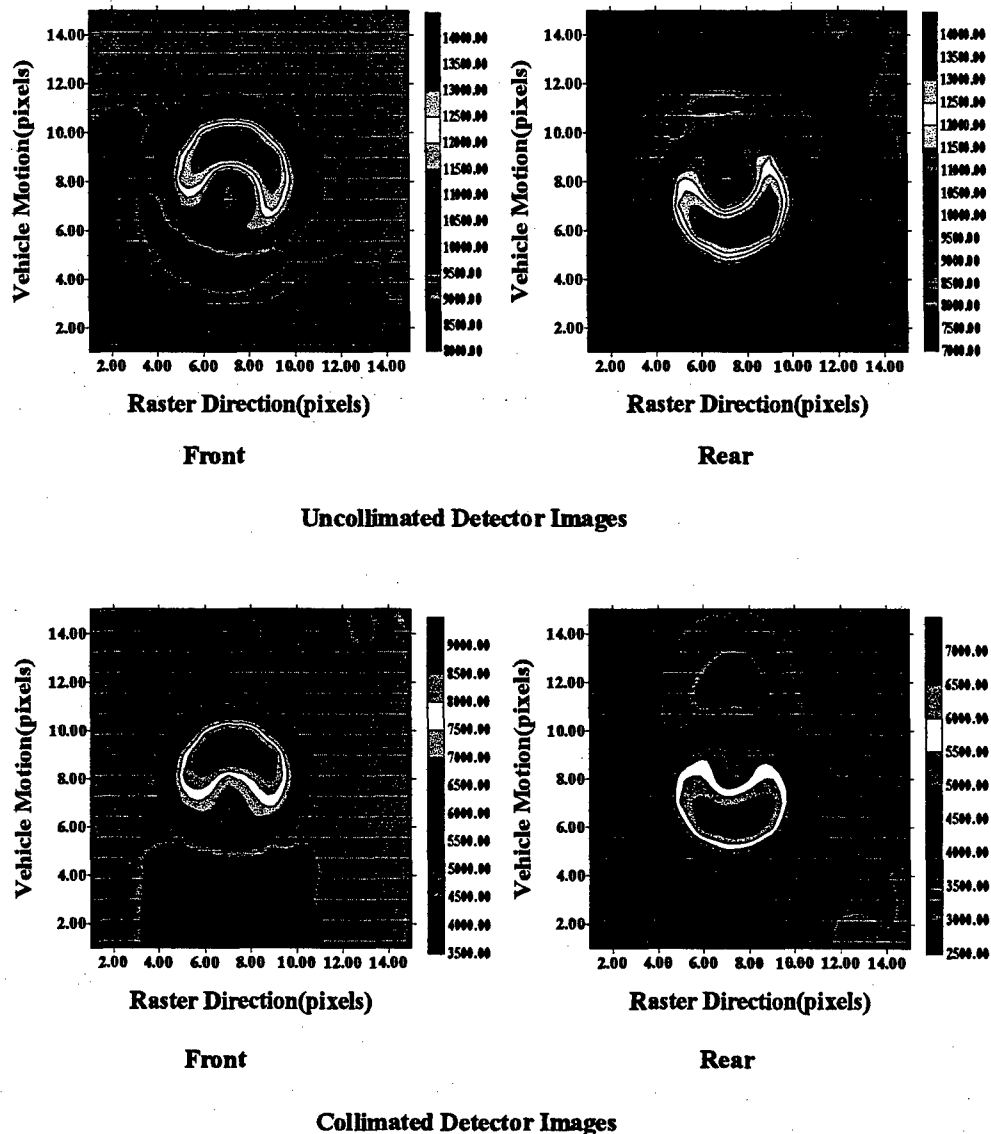


Figure 5. TS/50 antipersonnel mine, on surface, 15 mm resolution.



RATON
TECHNOLOGY
RESEARCH

The surface laid land mines can be easily recognized by both the shadowing effects and the vivid air volume signature in combination with the mine geometric shape in LMR images. In contrast the shallow buried mine emphasizes the air volume signatures and have no mine case shadow.

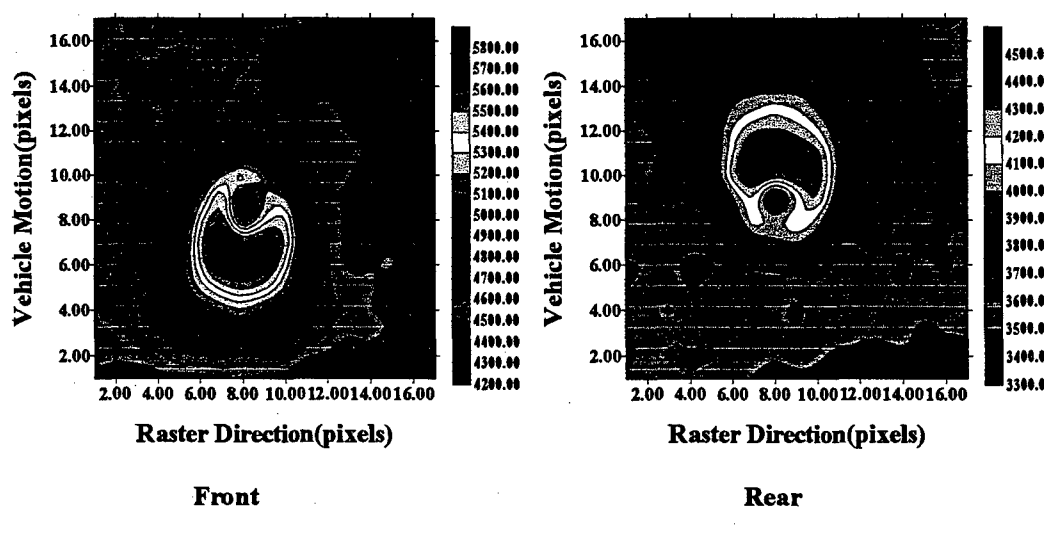
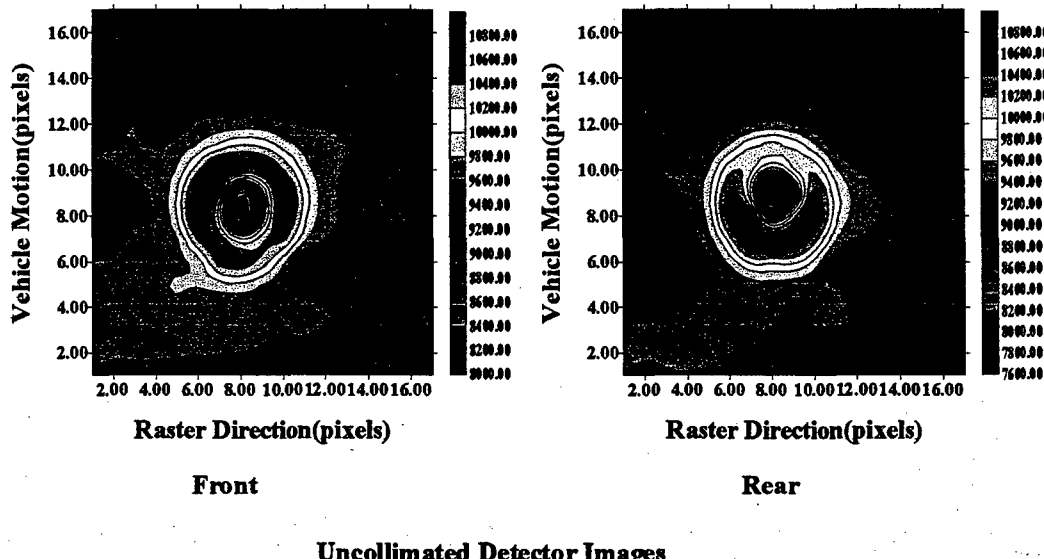


Figure 6. TS/50 antipersonnel mine, flush DOB, 15 mm resolution.



2. PROPOSED LMR SYSTEM DESIGN

2.1 General Configuration

2.1.1 LMR Vehicle Configuration

Because of the availability of suitable "off-the-shelf" x-ray generators (refer to section 4.2, where details are given), a compact LMR land mine detection vehicle can be designed and demonstratively fabricated. (see Figure 7 for a concept drawing of the LMR vehicle). This vehicle is about the size of a large lawn mower. Such an LMR detection system will include an x-ray generator with electric power requirements in the range of 50 W to 800 W, a compatible electric power generator for the x-ray generator, two uncollimated detectors and two collimated detectors which are made from plastic scintillator blocks, an advanced electronics system including a high performance computer with moderately fast data acquisition boards to achieve data transfer for computer image processing as well as pattern recognition. For this proposed system, raster direction scanning will be achieved by a rotating collimator around the x-ray generator tube head. The motion direction controlling system which provides control of that image axis will be the same RF or sonic x-y position system or Sonic x-y positioning system used by the RMPA system.

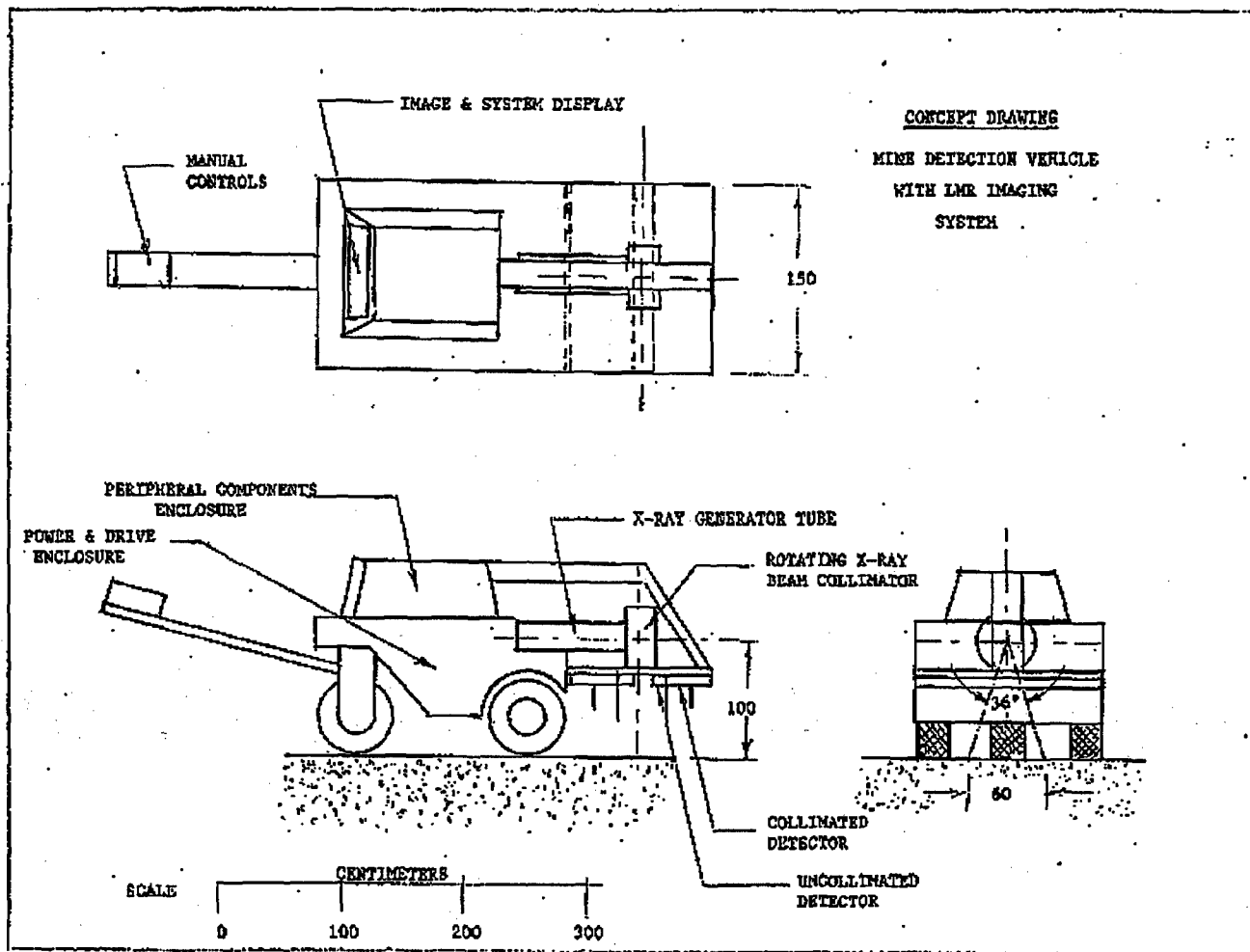


Figure 7. Concept diagram of LMR land mine detection vehicle.

2.1.2 Definition of Motion

During landmine detection by the multiple-sensor system, areas of suspected mines as determined first by the RMPA system will be marked with a color-code. Then, the LMR system will move to these areas and image them. The mines sought for are usually from 8 cm to 35 cm in diameter. The scanning area of these suspected spots will be either 20 cm by 20 cm, or 60 cm by 60 cm zones based on the color-code marked by RMPA which indicates the likely size and major axis of the suspected object.

As shown by both measurements and MCNP numerical simulations, in order to subdue photon quantum statistics in land mine detection, there should be at least two million incident photons per pixel. For a typical x-ray generator (including beam collimation), one joule of electric energy



per pixel is the generator requirement for a 15 mm by 15 mm illuminated pixel. Based on x-ray generator power and often-used 15 mm resolution. The interrogation time for a certain area by the LMR system can be predicted by the following equation:

x-ray power (watts) * dwelling time T_d (second/pixel) = 1 joule/pixel

$\rightarrow T_d = (1 \text{ joule/pixel}) / (\text{x-ray power in watts})$

With 100 W x-ray generator and 15 mm resolution, the calculation of interrogation time is as follows:

60 cm by 60 cm area:

Pixel number $N = (60 / 1.5) * (60 / 15) = 40 * 40 = 1,600$

1 joule/pixel with 100 W \rightarrow dwell time for each pixel $T_d = 0.01 \text{ second}$

Image interrogation time $T = T_d * N = 16 \text{ seconds}$

Vehicle motion speed $V_m = 60 \text{ cm} / 16 \text{ s} = 3.75 \text{ cm/s}$

20 cm by 20 cm area:

Pixel number $N = (20 / 1.5) * (20 / 15) = 13.3 * 13.3 = 177.8 \rightarrow 178$

1 joule/pixel with 100 W \rightarrow dwell time for each pixel $T_d = 0.01 \text{ second}$

Image interrogation time $T = T_d * N = 1.78 \text{ seconds}$

Vehicle motion speed $V_m = 20 \text{ cm} / 1.78 \text{ s} = 11.25 \text{ cm/s}$

This system x-ray beam trace on the soil surface is shown in the Figure 8.

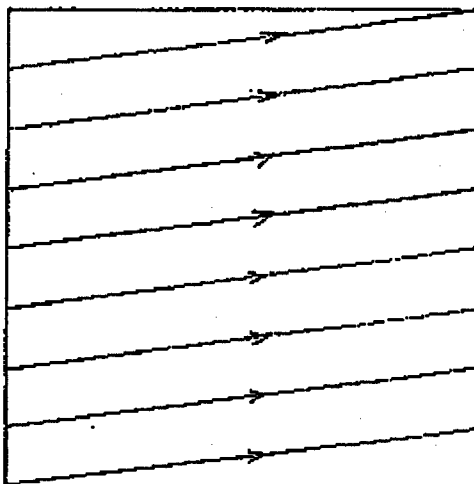


Figure 8. X-ray beam trace on soil surface.



Interrogation Area	20cm by 20cm	60cm by 60cm area
Image Interrogation Time (sec)	2	16
Vehicle Motion Speed (cm/s)	11.25	3.75

Table 1. Motion speed and image interrogation time for x-ray generator power at 100 W and 15 mm resolution.

2.2 X-ray Generators

2.2.1. LORAD X-ray Generators

A Lorad LPX-160 constant potential x-ray generator was obtained from one of the LORAD representative companies to more clearly simulate the generator type to be used in the actual detection vehicle. This x-ray unit has a tube head, a liquid cooling unit, a digital control unit and cables for power supply and liquid cooling (see Figure 9). The x-ray output is 5 to 160 kV at 0.1 to 5.0 mA constant in time (i.e. DC). The exit x-ray beam angle is 40 degree. Physical specifications of this x-ray generator module are given in Table 2.

Table 2. Lorad LPX-160 liquid cooled unit physical parameters.

System Component	Height(cm)	Width(cm)	Depth (cm)	Weight(kg)
Tube Head:	Length= 72.39	Diameter= 18.4		13.2
Control Unit:	30.5	45.7	26.7	15.9
Liquid Cooling Unit:	30.5	36.8	40.6	24.5

This module can be portable-generator powered, as can the other components of the land mine detection vehicle. The power level, dimensions and weights of the components of the x-ray module satisfy the requirement of easily available or fabricated components for the LMR land mine detection vehicle. The constant potential is achieved by monitoring voltage and current directly at the x-ray tube, which provides uniform x-ray output and far better reproducible output than the Maxitron 300 generator that is currently used at the University of Florida.

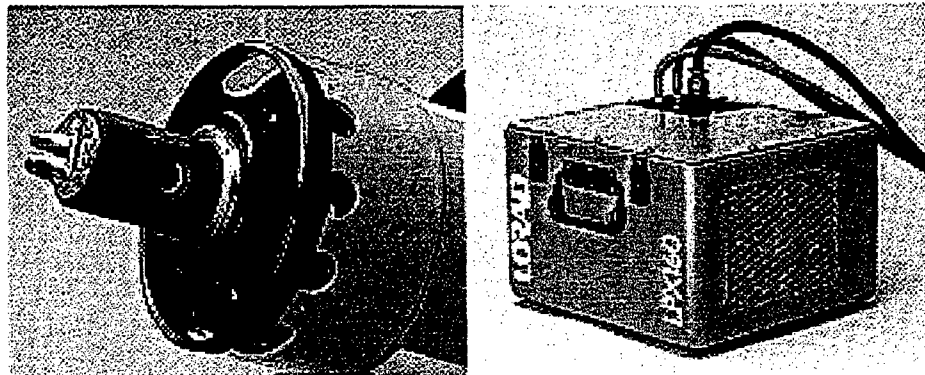


Figure 9. Lorad LPX-160 x-ray generator tube head and liquid cooling unit.

There is also an air-cooled version available called the LPX-200 (see Figure 10). The air-cooled module with no separate cooling unit, reduces the x-ray generator system weight by over 40% compared to the liquid-cooled unit. Table 3. gives the specifications of this module.

Table 3. Lorad LPX-160 air-cooled unit physical parameters

System Component	Height(cm)	Width(cm)	Depth (cm)	Weight(kg)
Tube Head:	Length= 77.5	Diameter= 18.4		15
Control Unit:	30.5	45.7	26.7	15.9

Quotations for Lorad LPX-160 and LPX-200 are \$19,500 and \$27,500 respectively.



Figure 10. Lorad LPX-160 x-ray generator air-cooled tube head and digital control unit.

A Measurement Comparison of the LORAD and Maxitron Generator LMR Capability. The x-ray generator currently used in the University of Florida LMR laboratory is a General Electric Maxitron 300 which was manufactured in the 1950's. The Maxitron 300 has a self-rectification current at 1,200Hz. Partly due to design, major structured fluctuation in x-ray output occurs due to variations in the electron focal spot shape and position. Therefore, the x-ray photon illumination for each pixel with this device has significant structured noise which is then found in the acquired LMR images. In contrast, the images obtained with the LPX-160 have little structured noise because of its constant (less than 1% fluctuation) potential design. A plastic disk with four holes of different diameters (see Figure 11) was employed as an LMR object using both the Lorad LPX-160 and Maxitron 300 as the illuminating x-ray source.

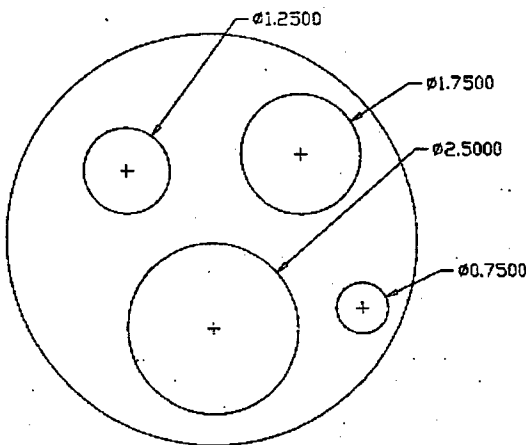


Figure 11. Diagram of 6 inches diameter plastic disk with four holes (diameters in inches).

Comparison of the images (see Figure 12.) shows that the Maxitron 300 images have the expected high noise relative to the Lorad LPX-160 images. Using a Lorad LPX-160, or a similar modern off-the-shelf constant potential x-ray module, will yield LMR images with a significantly smaller noise component than all the example mine images in this report which were all obtained using the Maxitron 300 generator.

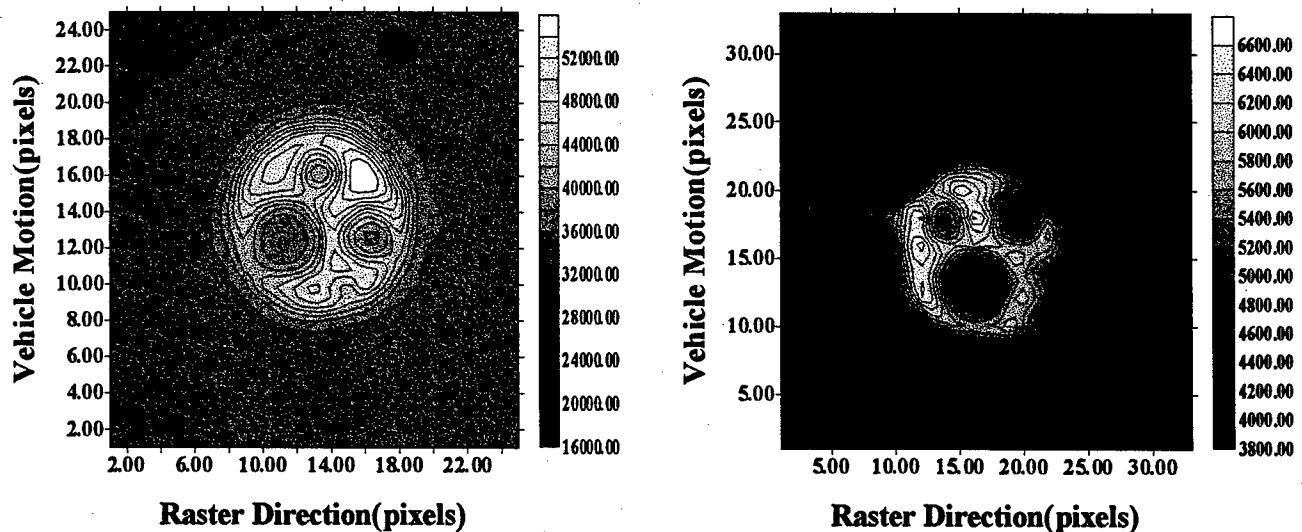


Figure 12. Plastic disk images obtained with Lorad LPX-160 (left) and Maxitron 300 (right).



The LPX-160 with a total weight of about 70 to 120 lbs not including the cables (which weigh about 20 lbs) should be easily integrated into a large lawn mower size vehicle, such as shown in Figure 7.

2.2.2. Aerosino AX160-2-15

Contact with x-ray generator manufacturers revealed another company's product that could be used in the LMR detection vehicle. The Aerosino AX160-2-15 x-ray module is a relatively low power x-ray generator, 70 to 160kV and up to 2mA adjustable current, with a maximum 180 W output using regular air cooling. It is a continuous duty, constant potential module. Because this unit has relatively low power, the price is also relatively low. The quotation for the Aerosino x-ray generator is \$3,000. However, the x-ray tube of an Aerosino AX160-2-15 is made of glass which is much more fragile than the ceramic tube of the Lorad LPX-160. Therefore, a complex shock absorbing structure would be needed for the Aerosino AX160-2-15 x-ray module and the requirement of a rugged generator and a simple, reliable system for mine detection work in the field probably makes the Lorad module a better choice.

2.3 Rotating Collimator

2.3.1. Configuration

In order to efficiently achieve raster direction motion, x-ray beam angle tilting has been chosen. This is achieved by attaching a rotating collimator to the x-ray tube head.

60 cm by 60 cm interrogation area:

Because the x-ray output distribution emerging from the generator is not uniform, a lead sheet with a hyperbolic shaped slot will be made and rolled into a cylindrical shape. This cylinder will be located coaxial with the x-ray tube head keeping the center of the slot aligned with the center of the x-ray output window. This allows for photon intensity compensation in a pixel scan. Outside of this cylinder, is another coaxial cylinder with ten equally separated holes aligned in the same section circle. Thus, there are 36 degrees between adjacent holes, which will be within the 40 degree of the emerging x-ray beam cone. These two cylinders together make a collimator which can yield equal illumination of each pixel in a scan line. The x-ray beam moves with constant linear speed on the soil surface in raster direction thereby (see Section 4.3.4.) ensuring the same photon illumination for each pixel. The raster direction scanning will be in a continuous mode with no dead time and the scanning is always from the leftmost pixel to the rightmost pixel (as illustrated in Figure 8). The scanning speed in the raster direction can be adjusted by changing the speed of the motor driving the outer cylinder to produce the dwell time required for each pixel. Including adjustment of the x-ray generator output power level, individual areas of interest marked in the RMPA interrogation can be



scanned by the LMR system at a variety of speeds. One such scan speed is presented in this report based on a fixed rotational speed of the generator collimation.

20 cm by 20 cm area:

The configuration of the rotating collimator is essentially the same as the one described above except that there are 30 holes equally separated and aligned in the same section circle on the outer cylinder which yields 12 degree interval between these holes and the hyperbolic slot in the inner cylinder subtends 12 degree from the focal spot of the x-ray tube head.

These two designs are merged into one rotating collimator assembly illustrated in Figure 13. During operation of the LMR land mine detection system, the operator will slide in or out this rotating collimator and meanwhile change the vehicle motion speed to satisfy the interrogation area requirements. Figure 14 and 15 show the details of the collimator.

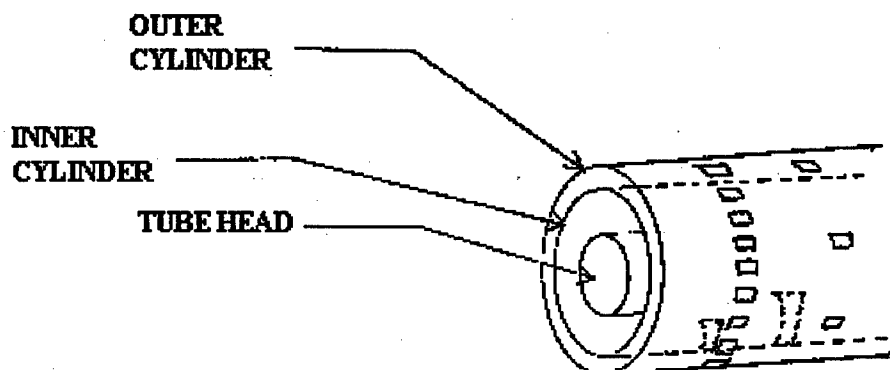


Figure 13. Side view of the rotating collimator.

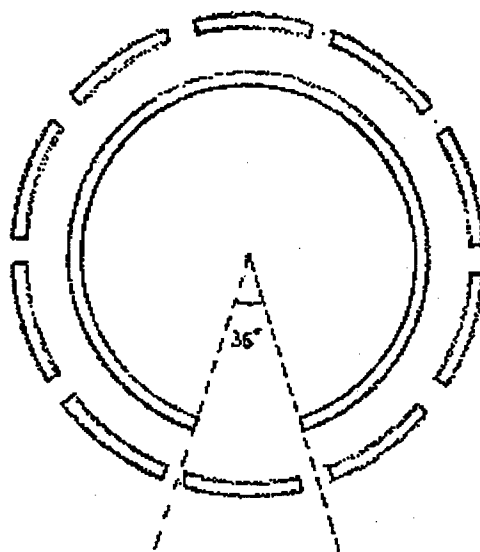


Figure 14. Cross section view of the rotating collimator.



Figure 15. Extended view of inner and outer cylinders of the rotating collimator.

2.3.2. Pixel Pattern and Diameter of Rotating Collimator

For the antitank and antipersonnel mine under consideration, 15 mm resolution (pixel size) is sufficient. When the x-ray beam scans from the leftmost pixel to the rightmost pixel (as illustrated), the x-ray spot on the soil surface will elongate when the illumination beam is not



perpendicular to the soil surface. Maximum elongated x-ray beam spot is at leftmost pixel or rightmost pixel (as illustrated). (see Figure 16). Even though the spot is elongated, the number of photons per pixel is still the same because of the rotating collimator design.



Figure 16. X-ray beam illumination pattern on the soil surface with rotating collimator.

As 15 mm by 15 mm will be the largest elongated x-ray beam spot on the soil surface, the required diameter of the rotating collimator can be determined. From the Lorad LPX-160 data, the focal spot is 1.5 mm^2 . The length of one side of a square focal spot is then approximately 1.2 mm. When the x-ray beam spot at the leftmost pixel, from the similar triangle theorem, the radius of the rotating collimator is calculated as follows (see Figure 17):

$$\begin{aligned} AC / AM &= 1.2 \text{ mm} / 15 \text{ mm} \rightarrow AC = AM * (1.2 / 15) \\ MC &= AM + AC = 1000 \text{ mm} / \cos(18^\circ) = 1052 \text{ mm} \\ \rightarrow AC &= 1052 \text{ mm} / (1 + 15 / 1.2) = 78 \text{ mm} \rightarrow AC = 8 \text{ cm} \end{aligned}$$

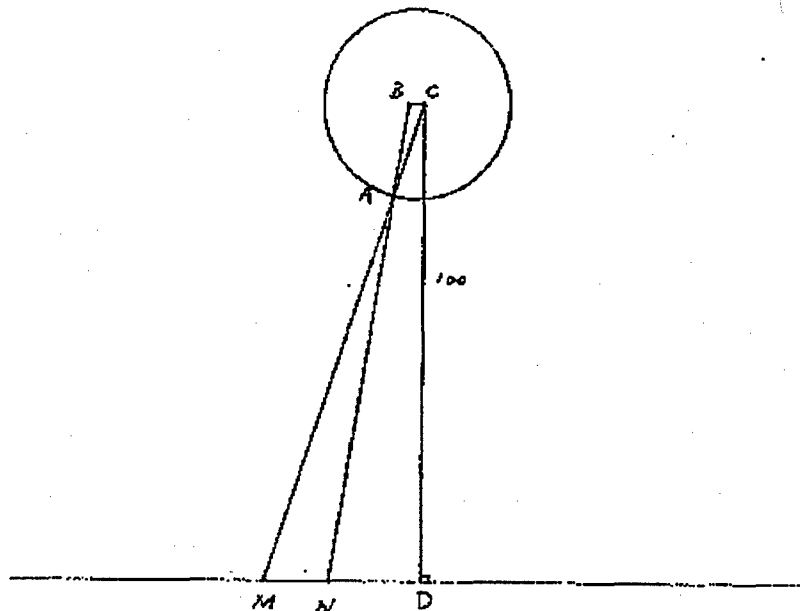
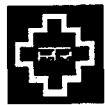


Figure 17. The rotating collimator diameter calculation diagram.

2.3.3. Angular Speed of the Rotating Collimator

With a 100 W x-ray generator, the required dwell time for each pixel is 0.01 second which determine the angular speed of the rotating collimator. Using the 15 mm pixel size, a 60 cm line scan (corresponding to 36 degree rotation of the collimator) is divided into 40 pixels. The 36 degree rotation must occur in 0.4 second which implies 4 seconds for one revolution of the rotating collimator. As we mentioned before, if the x-ray generator power is greater than 100 W, the same photon illumination occurs at higher scanning speeds.

2.3.4. Self-normalization of Pixel Dwell Time

There is another advantage to using this rotating collimator. As the x-ray beam scans one line of the interrogated area, the dwelling time of each pixel is the same. In Figure 18, the V_c is the horizontal speed of the center pixel and V_l is the horizontal speed of the leftmost pixel of one line. The following derivation demonstrates that V_c is equal to V_l .

$$OL = OC / \cos(\theta), V_l = OL * \omega * \cos(\theta) = OC * \omega = V_c$$

where ω is the angular speed of the rotating collimator.

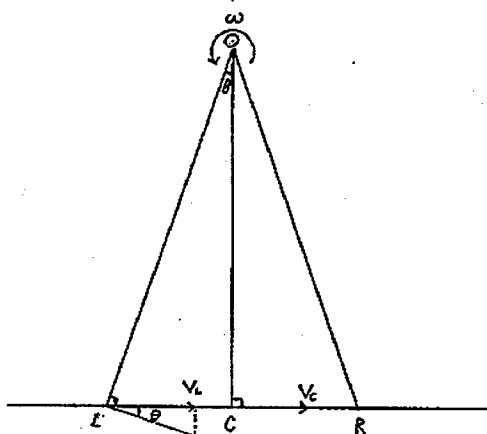


Figure 18. Dwell time calculation diagram.

2.3.5. MCNP simulation

MCNP simulation of the x-ray angle tilting has been accomplished. The buried simulated mine is clearly visible in both collimated and uncollimated detector images. In the MCNP simulations, cases where the mine is located both at the center and off the center of the source beam tilting angle sweep have been investigated.

In both cases, there are distortions in the mine images. The contours of the cylindrical mine in the images are no longer roughly circles (see Figure 20). The intensities, from the geometric center of the mine, drop more sharply in the raster direction than in the motion direction and the mines in the images appear to be compressed in the raster direction. This image distortion has been investigated and the mechanism is physically understood. Furthermore, an image distortion correction method has been obtained.

In the LMR system, image pixel locations are defined by the x-ray beam locations on the soil surface. For the case of an x-ray beam incident perpendicular to the soil surface, the point where the x-ray beam vertical projection hits the mine has the same pixel coordinate location as the source. For the x-ray beam angle tilting case, the incident beam location on the soil and the location of x-ray beam hitting the mine have different coordinates. Because x-ray beam angle tilting is in the raster direction, the geometric length of a buried object in the raster direction is represented by a smaller length in acquired images. In Figure 19, CD is the length in an LMR image, while AB, the actual length, is greater than CD.

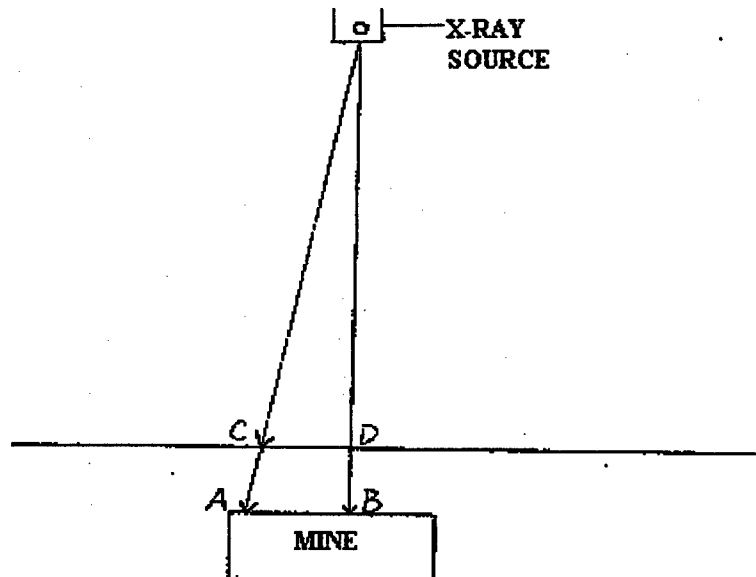
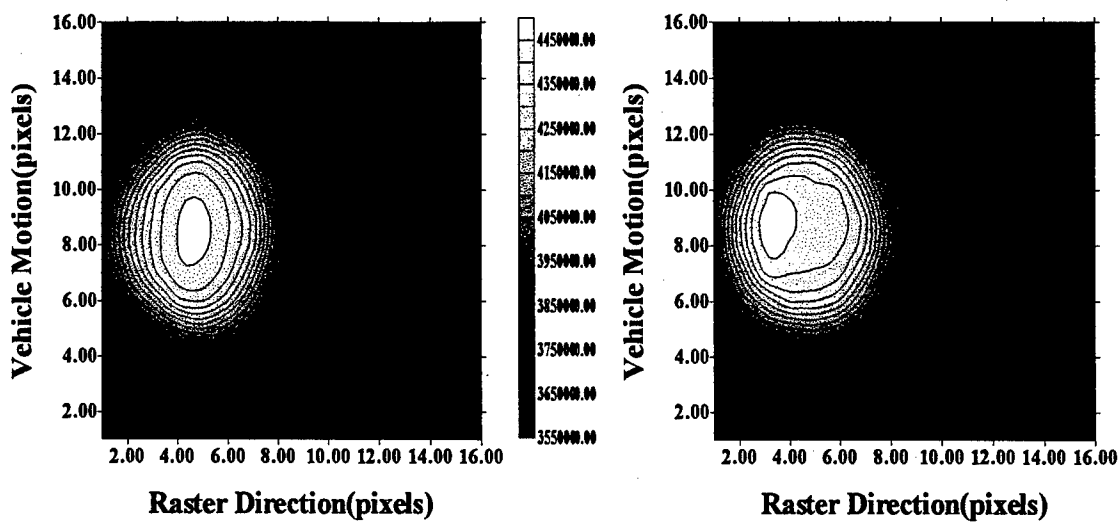
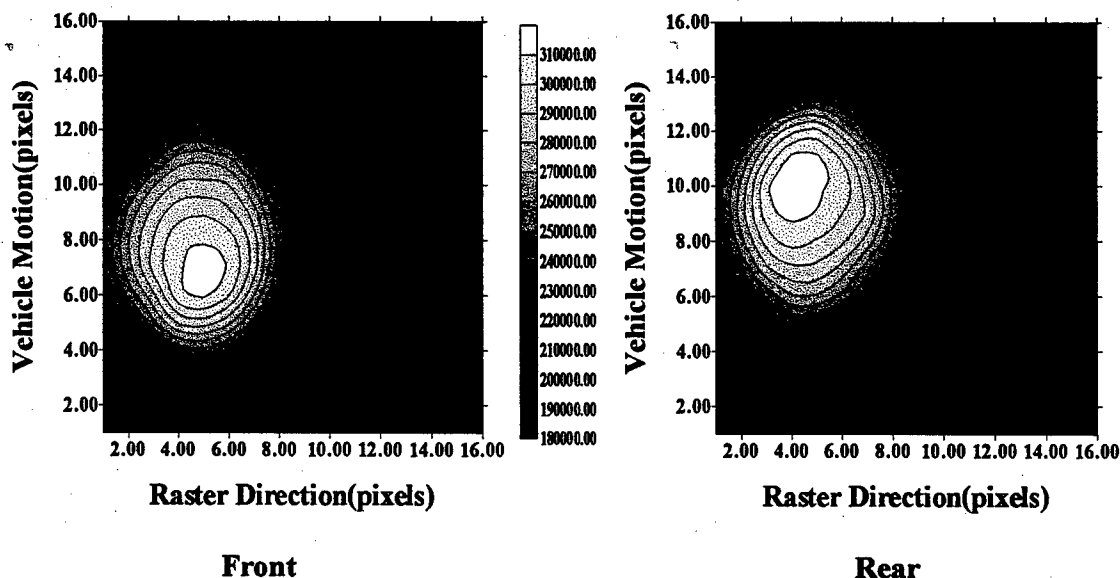


Figure 19: Illustration of raster direction distortion in LMR images by x-ray beam angle tilting.

Because the photon lateral migration effect (intensity shifting in the motion direction) in the collimated images is not affected by the raster direction x-ray beam angle tilting and the LMR system detector sets are symmetric, there is a method to correct the raster direction distortion caused by the x-ray beam angle tilting. The two collimated detectors of an LMR system predominantly sense multiple-collision photons. The lateral migration effect is readily apparent in collimated detector images because the maximum intensity value of the buried mine in the images shifts away from the geometric center of the mine. This shifting is proportional to the depth-of-burial. An empirical correction can be acquired through detection of objects at known different depths-of-burial. With this empirical correlation, the shifting distance in the collimated detector images can be measured and then used to calculate the depth-of-burial of the object. Once the depth-of-burial is estimated, we can use a simple geometric projection formula to correct for the raster direction distortion.



Uncollimated Detector Images



Collimated Detector Images

Figure 20. MCNP simulated images of a solid mine off-center of the image.



In the simulation setup, the surface of the soil is smooth, but in the Figure 20 images, there are some ridges in the background. In order to test whether these ridges are caused by the x-ray beam angle tilting or statistical reasons, the number of photons per pixels was increased from the value 1 million used in Figure 20 to 16 million. The resulting images in Figure 21 show that the ridges have almost disappeared.

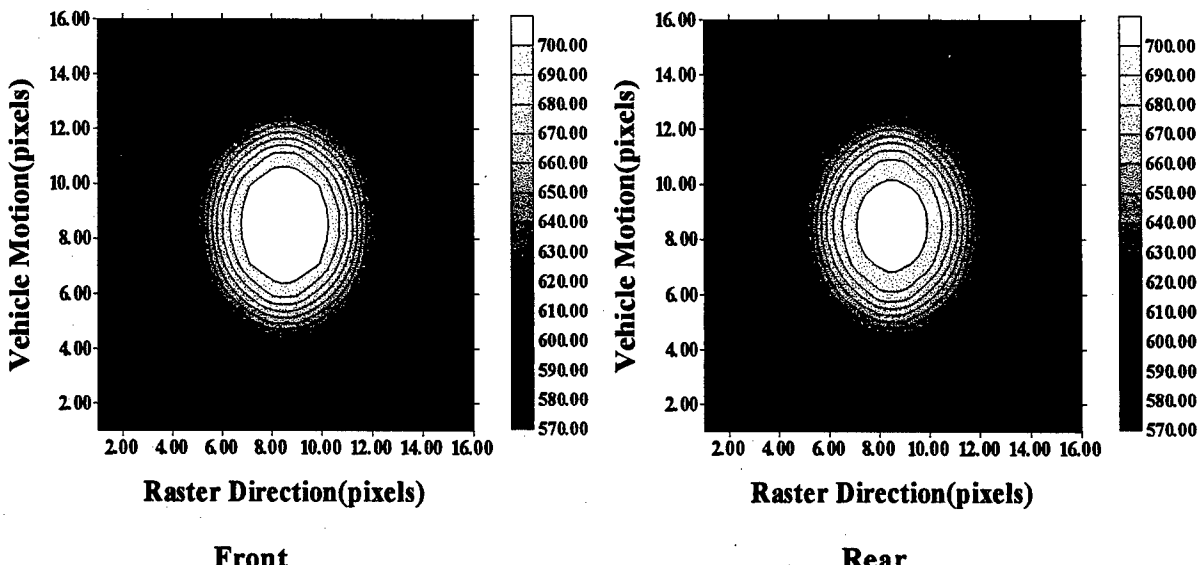


Figure 21. MCNP simulated images (uncollimated) with mine at the center of the images.

2.4 Detector Design and Optimization

Detectors are crucial components in the LMR land mine detection system. With well-designed and high performance detectors, the system can maximize the detection possibility and be made more compact to function more efficiently in the land mine detection environment. In the LMR system, high performance organic scintillator screen detectors (such as manufactured by Bicron, Inc) will be used as both collimated and uncollimated detectors. The uncollimated detector size is about 100 cm long, 5 cm wide and 2.5 cm thick. The collimated detector size is about 100 cm long, 20 cm wide and 2.5 cm thick. We have two options for detector design.

2.4.1 Multiple Miniature Photomultiplier Tubes Case

In this detector design, there will be about 20 miniature photomultipliers with miniature amplifier/high-voltage suppliers coupled with each detector and they will be arranged at every 4 inches along each side of the detector.



2.4.2 Single Photomultiplier Tube with Light Pipe Case

This design is more cost effective. For each detector, one photomultiplier tube will attach to the end of the scintillator via a light pipe. Bicron, Inc. suggested this option.

2.5 Image Acquisition and Processing

2.5.1 Color Coding and Image Acquisition

In the multiple-sensor system, the RMPA system will scan the field first. As suspected target objects are detected, the RMPA system will mark the predicted center or major axis of the objects by different colors based on the sizes of these objects. Currently we differentiate the objects into two major categories: less than 13 cm in diameter or major axis extent and greater than 13 cm in diameter or major axis extent. For less than 13 cm objects, there will be a big red dot at the center of these objects. For greater than 13 cm objects, if the objects are circular or square, a yellow dot will mark the centers; otherwise, yellow lines along the major axis of these objects will be marked on the soil surface. For less than 13 cm objects, the scan area will be 20 cm by 20 cm; for greater than 13 cm objects, the scan area will be 60 cm by 60 cm. Most mines can be covered by a 60 cm by 60 cm area with more than adequate margins. If special objects are found, such as a long length rectangular object, several 60 cm by 60 cm squares will be considered if warranted by the situation of the mine field. When scanning different size areas, different set of slot and holes on the rotating collimator will be used. For a 20 cm by 20 cm area, the 30 holes and 12 degree slot is aligned with the x-ray output window. For a 60 cm by 60 cm area, the 10 holes and 36 degree slot will be slid out and the requisite corresponding motion speed of the LMR vehicle will be selected.

Because LMR images are the horizontal projected images of all the detectable objects in or on the soil, the processing of these images will concentrate on image enhancement, image segmentation, image labeling, image correlation and pattern recognition. In the LMR system, image enhancement is achieved by low pass filtering. Because the LMR land mine detection system is a system composed of electronics, detectors and an x-ray generator, there are various noises in the acquired LMR images and the images are corrupted by some random variations in intensity values. Since the sizes of the mines are usually above 8 cm (3 inches), spatial and frequency low pass filters are applicable. The commonly used low pass filters are mean filters, median filters and Gaussian filters. These low pass filters can remove statistical noise and some small surface irregularities. Mean filtering can be achieved by eight-connected neighborhood averaging; the mean filter mask is shown in Figure 22.



1/16	1/8	1/16
1/8	1/4	1/8
1/16	1/8	1/16

Figure 22. Mean filter mask.

Median filtering is achieved by replacing each pixel value with the median value in the local neighborhood. Gaussian filtering is similar to mean filtering but the values in the mask are obtained from the two dimensional Gaussian function.

2.5.2 Image Segmentation and Labeling

In a LMR image of a landmine detection field, there will be a lot of objects in the images, such as potholes, rocks, tree trunks and mines, etc.. In order to differentiate them and apply image correlation to eliminate the non-mine objects, image segmentation and labeling is necessary. Image segmentation can be accomplished by a histogram thresholding method. The commonly used methods are iterative histogram thresholding, adaptive thresholding and variable thresholding methods. After thresholding, the result image is a binary image. We can then use an eight-connected neighborhood iterative method to label the objects in LMR images. These labeled binary images will serve as a map for image processing of each object in the LMR images.

2.5.3. Image Correlation Processing

From each detection run, there are four images of the suspected area: front uncollimated detector image, rear uncollimated detector image, front collimated detector image and rear collimated detector image. Because of the LMR system set-up, these images have strong correlation between them.

The uncollimated detector images have surface features and the collimated detector images have both surface features and subsurface features. Therefore, surface feature removal can be accomplished by manipulating the collimated and uncollimated images (see Figure 23).



RATON
TECHNOLOGY
RESEARCH

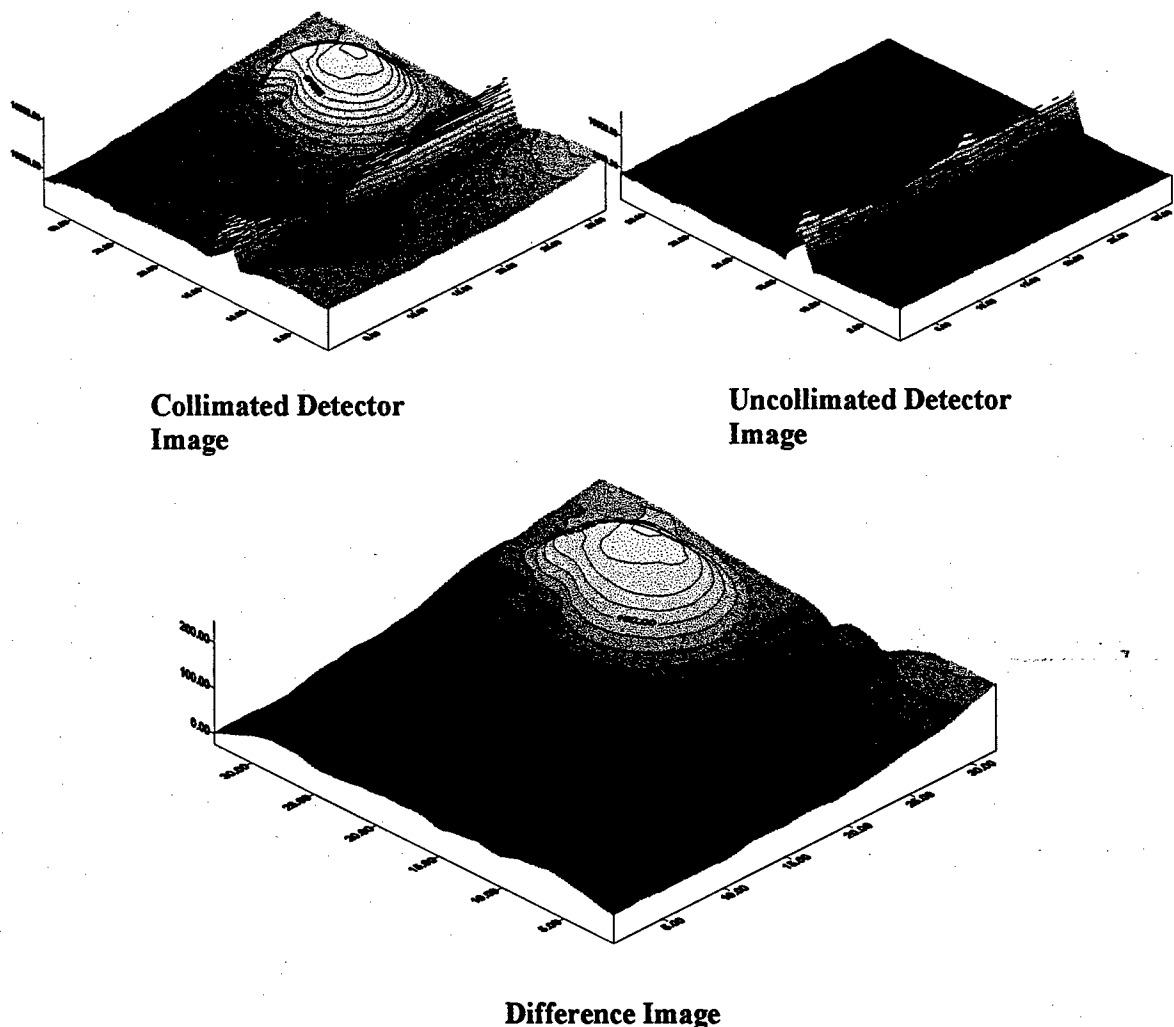


Figure 23. Surface features removal illustration.



Using image correlation processing, slopes in LMR images can also be eliminated (Figure 24).

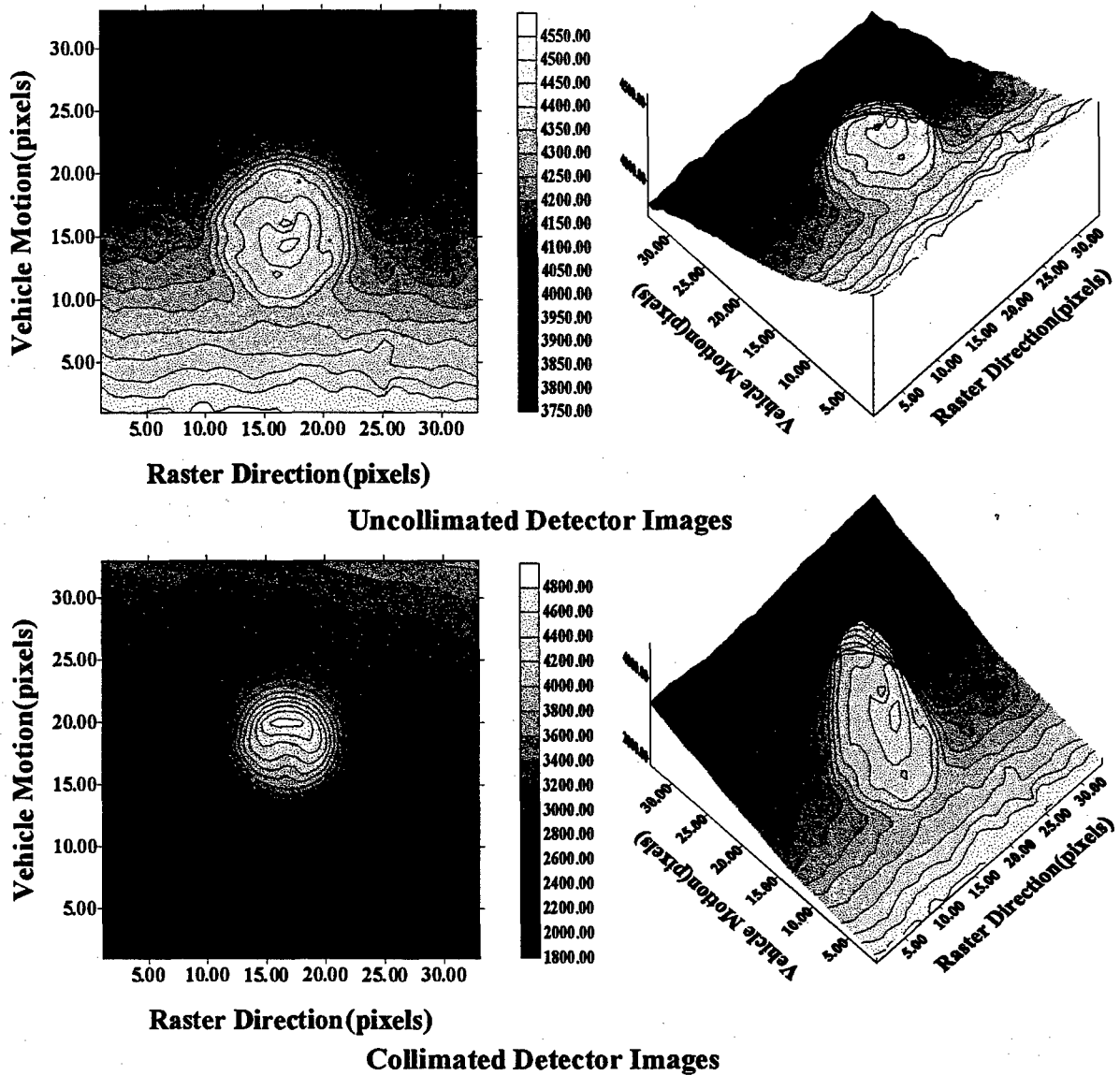
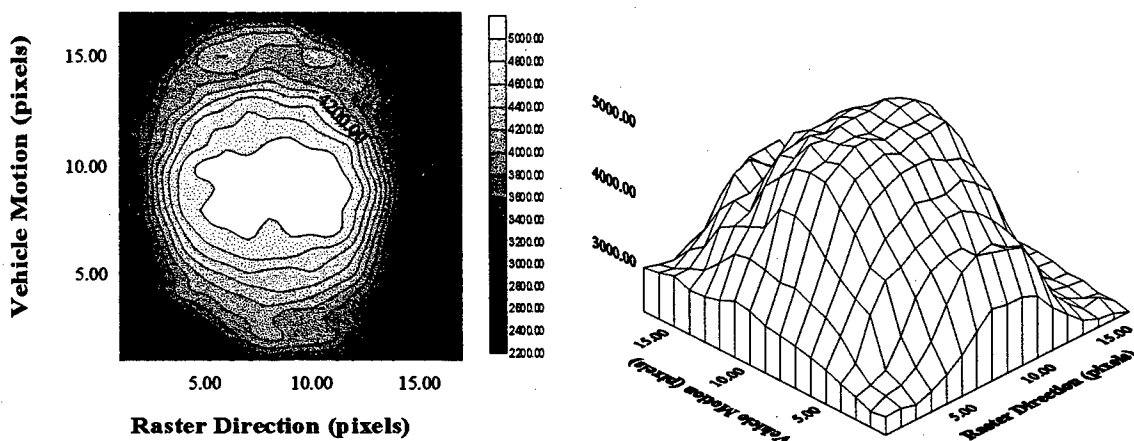


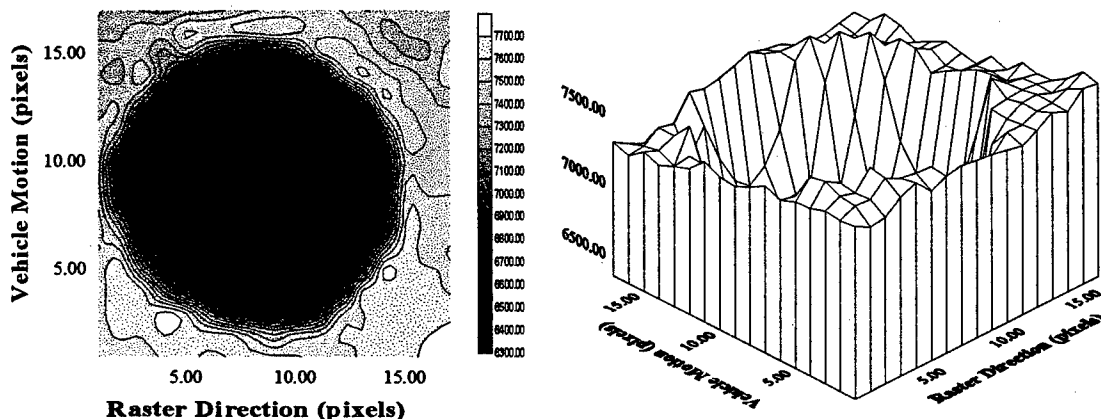
Figure 24. LMR images of a plastic mine buried with slope surface.



Because of the LMR detector design and the different photon interaction cross sections of different objects, the responses of the same object can be different in the uncollimated and collimated detectors. For plastic mines, the responses in all detector images are higher intensities than the responses of the soil. In contrast, the metallic mines have lower intensities in all detector images. For potholes, the response in uncollimated detector images is an intensity decrease while in collimated detector images there is an intensity increase. (Figure 25) Therefore, correlation between uncollimated detector images and collimated detector images is necessary to minimize the false positives.



Collimated Summed Detectors



Uncollimated Summed Detectors

Figure 25. LMR images of a pothole.



One of the LMR image characteristics is the lateral migration shifting of detected objects in the collimated detector images. The shifting in the front detector image is opposite to that in the rear detector image. The amount of shift is proportional to the depth-of-burial of the object and the depth-of-burial can be estimated from the shifting. Because there is symmetry in the collimated detector design, the amount of shift should be the same in both the front and rear collimated detector images. A simple average between these two images will give the physical (x, y) location of the object. By observation of known depth experiments, an empirical relation factor between the shifting and the depth-of-burial (z location) of an object can be obtained. Furthermore, this factor can be used for the correction of image distortion caused by the x-ray beam tilting.

2.5.4 Mine Identification

Air volume features combined with the geometric shape of the land mines in the LMR images should not only provide for mine detection with a near zero false negative rate but also make mine type identification highly probable and provide a near zero false positive alarm rate. Two kinds of landmine identification algorithms will be developed: template matching and pattern recognition through a neural network.

Template matching requires the original mine image data be stored in a computer in a certain format and that each acquired image is checked by the image template matching. An image with a template matching output value above a certain threshold value is expected to have a landmine in it.

Suppose that we have acquired LMR images of mines at known depths-of-burial and take them as templates. After we estimate the depth-of-burial by the amount of shift of the object in the collimated detector images, we apply the mine template for the right depth-of-burial to the acquired images. By using normalized cross-correlation and a certain threshold value, the center of mine in the images will yield the local maximum.

The template matching function is given by:

$$M[I, J] = C_{fg}[I, J] / \left\{ \sum_{k=1}^m \sum_{l=1}^n T[k, l] * F[I+k, J+l] \right\}^{1/2}$$

where $C_{fg} = \sum_{k=1}^m \sum_{l=1}^n T[k, l] * F[I+k, J+l]$ is a cross-correlation function
 $T[I, J]$ represents the mine template
 $F[I, J]$ is the acquired image

M will yield the maximum value right at the mine center in the acquired image. By applying a certain threshold value for the local maxima, the mine will be detected.

Pattern recognition through a neural network is a relatively new and complicated method. It requires a lot of known results of LMR image data, and uses these data to train the neural



network to achieve the optimized parameter configuration for landmine identification. The essence of this method is described as follows:

The neural network is composed of multiple layers, and in each layer we have certain nodes which can be interpreted as variables. A full permutation of weight factors which can be interpreted as coefficients connect the nodes of the adjacent layers. The number of layers of the neural network is selected according to the specific problem. By using a great number of LMR image data of known mines at different depths-of-burial, the weight factors can be optimized. Then we can use this neural network to detect land mines in LMR images.



3. Resonant Microstrip Patch Antenna

3.1 RMPA Principles

Recent theoretical and controlled laboratory studies provided direct evidence that a new type of fast responding (milliseconds) nonintrusive electromagnetic wave sensor can be applied in the detection of subsurface objects. The Resonant Microstrip Patch Antenna (RMPA) sensors are constructed with high conductivity metal layers on each side of a thin dielectric layer. RMPA, developed by Raton Technology Research (RTR) and NASA Johnson Space Center (JSC), has been extensively investigated for the detection of small nonmetallic antipersonnel land mines.

The newly developed RMPA sensing technology can be modeled as a high-Q resonant cavity that capitalizes on its resonant sensitivity to changes in overlying layer physical and electrical parameters. Both resonant frequency and impedance of a high-Q microstrip patch antenna are highly sensitive to coal layer thickness. The high-Q cavity is formed by a circular copper patch and ground plane. The physics principles of the RMPA will be described in the following paragraphs.

The RMPA sensor can be modeled as a high-Q cavity that capitalizes on its resonant sensitivity such that a distinct advantage is obtained over a nonresonant EM wave sensor. The wall of the high-Q cavity illustrated in Figure 26 is formed by the circular copper patch and the ground plane. The E-field within the cavity is excited/sensed by a vertical "probe" at the feedpoint. The TM_{11} mode E-field within the cavity and the fringing E-fields are illustrated by arrow symbols. The magnetic (H) fields are not shown; however, they are orthogonal to the E-fields and form the magnetic wall enclosing the cavity. The fringing E-fields (and H-fields) play an important part in the RMPA. The fringing EM fields are the coupling mechanisms between the internal cavity fields and external fields.

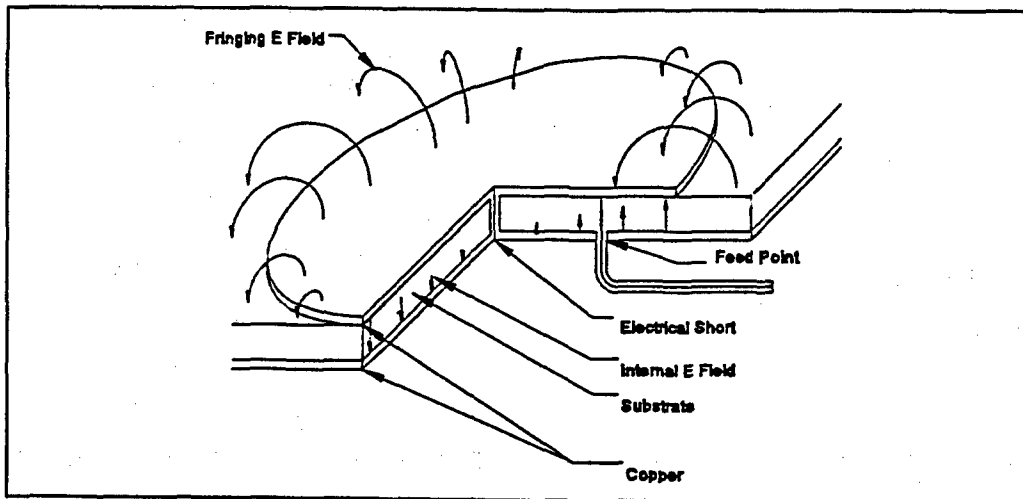


Figure 26. Vertical cross section of the RMPA sensor including electric field lines.



The fringing E-fields cause a polarized electromagnetic field to propagate from RMPA and into the dielectric coal layer. The E-field is predominately polarized along the axis through the feedpoint and electrical short. The radiation pattern is null at right angles to the axis. In the RMPA system, the primary field energy propagates upward from the antenna. It is important to realize that the E-field is essentially tangential to the layer being sensed. The reflection coefficient due to a difference in electrical parameters at each layer boundary can be determined. This gives rise to sensing signal.

The single high-Q RMPA transmits primary EM fields and senses the reflected and scattered secondary fields through its altered resonant condition. A continuous wave (CW) is emitted from RMPA and is partly reflected and partly transmitted at the soil-mine interface. The transmitted portion of the wave is reflected from the discontinuity in electrical conductivity and dielectric constant resulting from the occurrence of a buried object

The return signal to the RMPA is coupled through the fringing field and alters the E-field at the feedpoint. The E-field produces a voltage at the feedpoint and when divided by the current results in an impedance (ohms law). The returning electric field changes the feedpoint impedance. The microprocessor-controlled electronics change the frequency until the measured impedance is real. This is the resonant frequency of the sensor. The resonant impedance is measured and changes by a significant amount when the coal thickness changes. The real (R) and imaginary (X) values of the RMPA feedpoint impedance were measured over a range of frequencies with an HP 4191A RF impedance analyzer. The measured data is presented in Figure 27.

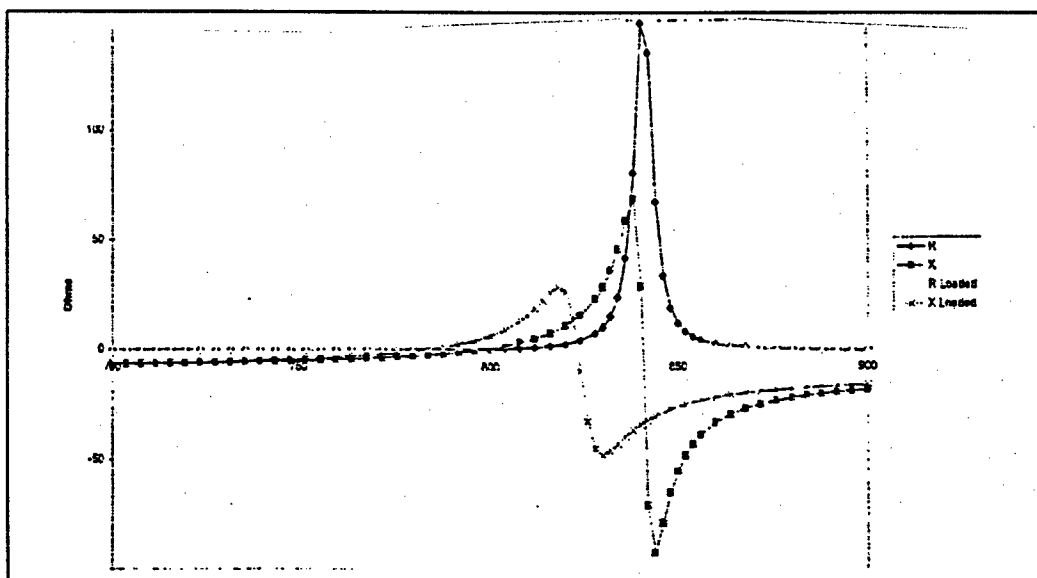


Figure 27. Measured 850 MHz RMPA sensor feedpoint impedance versus frequency.



The resonant impedance (ohms) curve to the upper right (A) was measured with the RMPA sensor radiating into free space. The lower left curve (B) was measured when RMPA was pressed against a low conductivity coal layer. The real (R) component (resistance in ohms) of the feedpoint impedance versus frequency curve illustrates the resonant characteristics of the high-Q cavity. The resistance rapidly changes on each side of the resonant frequency. The imaginary component (X) rapidly changes in the neighborhood of resonance. RMPA derives its sensitivity from the slope of the impedance characteristic in the vicinity of resonance. A slight change in frequency causes a significant change in impedance.

A resonant sensor loop of wire was originally investigated by David Chang in his Ph.D. work under R. W. P. King at Harvard. Later, Chang and Wait present the antenna input admittance dependence on layer characteristics in analytical form. They define the admittance of a resonant antenna as the current at the feedpoint divided by the applied voltage. This is mathematically given by:

$$Y = \frac{I}{V} = G + jB = I_o + 2 \sum_{m=1}^{\infty} I_m \cos m\phi; \\ I_m = j120 \pi^2 (a_m^p + a_m^s)$$

where G = the input conductance of the antenna,
 a_m^p = the primary contribution of an isolated antenna with no adjacent layered media,
and a_m^s = the contribution due to the adjacent layered media.

The Chang-Wait equations describe the antenna input admittance in the presence of a layered half space and were originally applied to uncut coal layer thickness. By using transcendental equations to define a_m^p and a_m^s , as the layer thickness increases, G oscillates around a value G_c with a decaying amplitude. As the thickness increases to a very large value, the value of G converges to G_c .

3.2 Land Mine Detection

Since the EDIT land mine detector will often scan over non-uniform surfaces, causing the height of the sensor head above the ground to vary, the question of height measurement naturally arises. If the height were known, then the data processing algorithms can account for height variation. The test data shows that for frequencies in the 850-MHz band, the measured resonant frequency and impedance versus height characteristics are consistent for both sand and clay soils. These data can be used in a calibration algorithm. The detection sensitivity for two different RMPA resonant conditions was investigated. The resonant conditions are:

- Resonant in free space: Impedance Techniques (RSZ and RMZ) Real (Z_r) and imaginary (Z_i) parts of the feed-point impedance are measured at constant frequency (F_a)



- Resonant when pointing into the soil: Resonant Technique (RZ) The resonant frequency (F_r) and resonant impedance (Z_r -real part) are measured

The free space resonant condition is important in that impedance measurements can be made an order of magnitude faster because resonance is only determined during calibration. Another issue relates to the possible differences in sensitivity between rectangular and circular patch antennas. The detection sensitivity is complicated by the standing wave's variation with both frequency and burial depth.

3.2.1. RMPA Detection Sensitivity

The detection sensitivity of RMPA is defined as the change in resonant frequency and impedance as RMPA is swept over a buried object. This report will attempt to determine whether the EDIT Land Mine Detector needs to measure both resonant frequency and impedance during every sampling event, or operate at some calibrated constant frequency, such as the free space (free space) resonant frequency and only sample the impedance components. Controlled laboratory tests have been conducted at Raton Technology Research, Inc. (RTR) to characterize circular as well as rectangular RMPA patch designs. These tests were designed to explore the sensitivity of the RMPA patches, as well as provide critical data to aid in the development of the EDIT system hardware and operational algorithms. The goal of the experiments was to determine electrical properties for a variety of soil conditions, target land mine types, and RMPA designs in an attempt to optimize the detection system. These properties include real and imaginary components of impedance, resonant frequency, and resonant impedance.

The RMPA antennas used were a circular patch of resonant frequency 888 MHz, and a dual feed-point rectangular patch of resonant frequencies 635 and 838 MHz. Both patches possess dielectric constants of 3 and are composed of copper sheeting over a dielectric media and were designed and manufactured by NASA.

Although the target simulants were non-metallic anti-personnel land mines, a metal land mine simulant was also included in laboratory tests. The metallic land mine simulant predominated the non-metallic response. The conclusion drawn from the data is that EDIT is a sensitive metal as well as non-metallic land mine detector. The data confirms that the detection sensitivity increases as water percentage (by weight) increases and soil grain size decreases in the soil surrounding the land mine. The data also suggests that the detection sensitivity increases with frequency. The sensitivity at 635 MHz was less than the detection sensitivity of 850 MHz antenna. Either the real or imaginary parts of the impedance reach a maximum over the land mine target. This behavior suggests that an algorithm that would square the real and imaginary parts and sum together would maximize the results over the target. Figure 28 shows the RMPA impedance response of three different frequency patches over a PMA-3 non-metallic antipersonnel land mine.

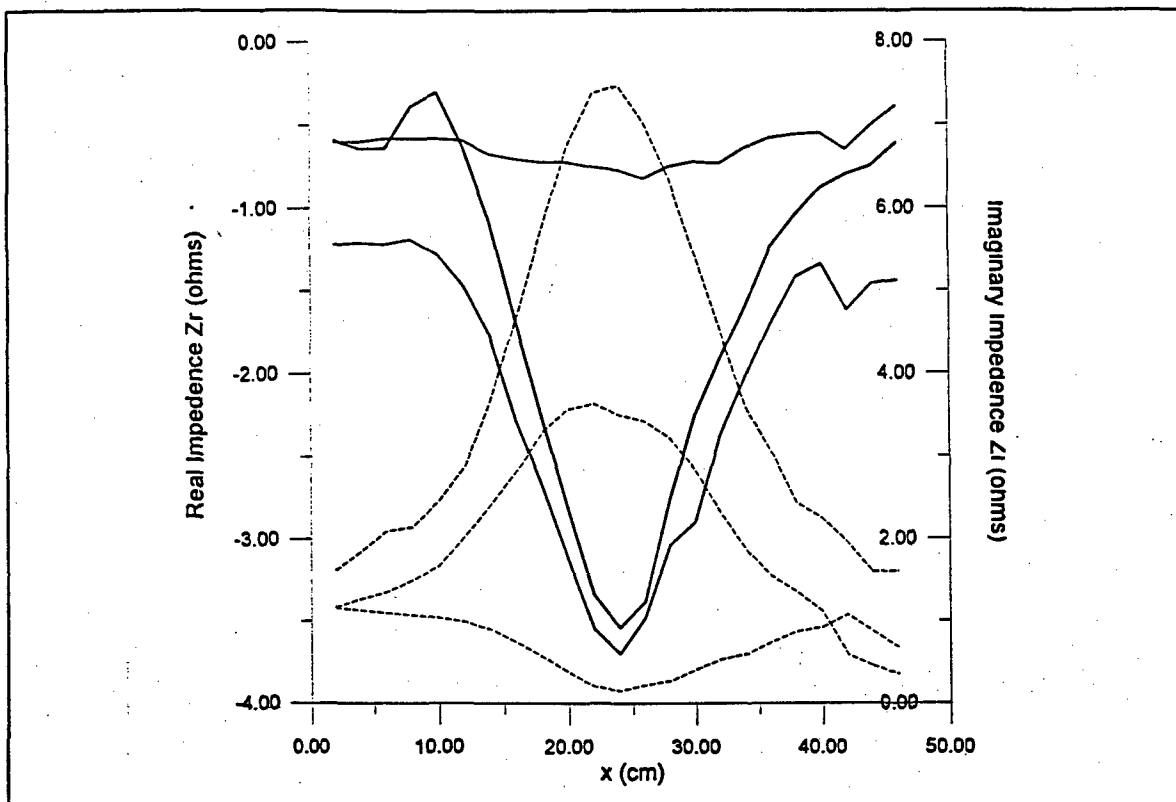


Figure 28: Frequency comparison of RMPA impedance response to a plastic mine at 5 cm depth in 1% moisture sand.

The experimental conditions tested included sand samples of variable moisture content. As well as moisture percentage, the degree of salinity was also variable. Several extreme comparisons of mine detectability were made including that of dry sand to saturated fresh water sand, and that of moderately saline sand to super-saturated brine water sand. The results of the tests indicate that it is not the presence of water that may decrease detection sensitivity, but rather the presence of ionic solution resulting from salt content. The greater the salinic molality of the saturating fluid, the greater the load on the resonant patch. The only way to combat this patch over load is by increasing the average offset distance of the patch to the ground. This greater offset distance creates a decrease in the magnitude of a land mine's electrical anomaly and thus its detectability wanes as well. However, for saline conditions at normal saturation levels, the detection sensitivity decreased very little in both the metallic and non-metallic land mine scans.



3.2.2. RMPA Antenna Development

The di-electric 10.2 antenna patches, received from NASA, have been tested in the laboratory target sand tubs. These two patches are dual-feed antennas constructed of a thin 25mil di-electric substrate and have resonant frequency parameters of 468/302 MHz for the rectangular patch, and 821/616 MHz for the square patch. During testing, both the height response and detection sensitivity were examined and compared to that of the di-electric 3 patches. The conditions for comparison include target burials of 0 to 5 cm and soil types of sand at 0% moisture and clay sediment at 10% moisture.

In comparing the detection sensitivity of the two new patches it was obvious that the smaller sized high frequency antenna (821/616 MHz) possessed the greatest sensitivity to anti-personnel mine targets at normal depths of burial and antenna stand-off distances. This results from the narrower aperture and wavelength of the patch's radiating field. The height response of this patch was also of considerably high quality in both repeatability and phase response. The most significant observation made during soil tests with the new antenna was the textbook response to various targets including mines, voids, and mounds, as well as the consistent ability to distinguish between all of the above. In comparing the magnitudes of the real and imaginary components of patch impedance during free space resonance during the soil scans, the absolute sign of the impedance variation provided direct evidence as to the target type. For example, both components are positive over an open soil void, both components are negative over a mound structure on the surface, and the components are of opposite sign for a land mine target which is essentially a buried void. The specific sign convention of the components aids in the estimation of the mines burial depth. For the 821 MHz measurement, a positive real part and negative imaginary corresponded to a shallow burial (0 to 2 cm) and the opposite sign convention indicated a deeper burial depth (3 to 6 cm). It follows that this behavior is probably cyclical with increased burial depth as determined through basic wavelength analysis, with decreases in magnitudes and increases in anomaly width also resulting. Figure 29 shows the impedance anomalies for a soil void and surface mound using the 821/616 MHz di-electric 10.2 RMPA patch.

In comparing the two different di-electric resonant patches (di-electric 3 and 10) in contention for the standard operating antenna in the EDIT detector, it was vital examine the detection sensitivity of the two different dual-feed rectangular patches. The 3 di-electric patch operated at 835/635 MHz and is twice the size and weight of the 10 di-electric patch at 821/616 MHz. However the larger patch showed greater versatility for detection of targets over a great range of soil types and moisture conditions which in specific instances the smaller patch provided more sensitivity and resolution. Therefore it has been decided to continue using both patches, alternately, for preliminary testing within the sensor head enclosure. It has also been decided that an addition antenna with a higher lower band will be built such that the patch's low end will run in the 660 to 680 MHz range instead of the low 600's. This is necessary due to the operating range of the new CFS/D's voltage control oscillator. This will not affect the detection capabilities or system development schedule.

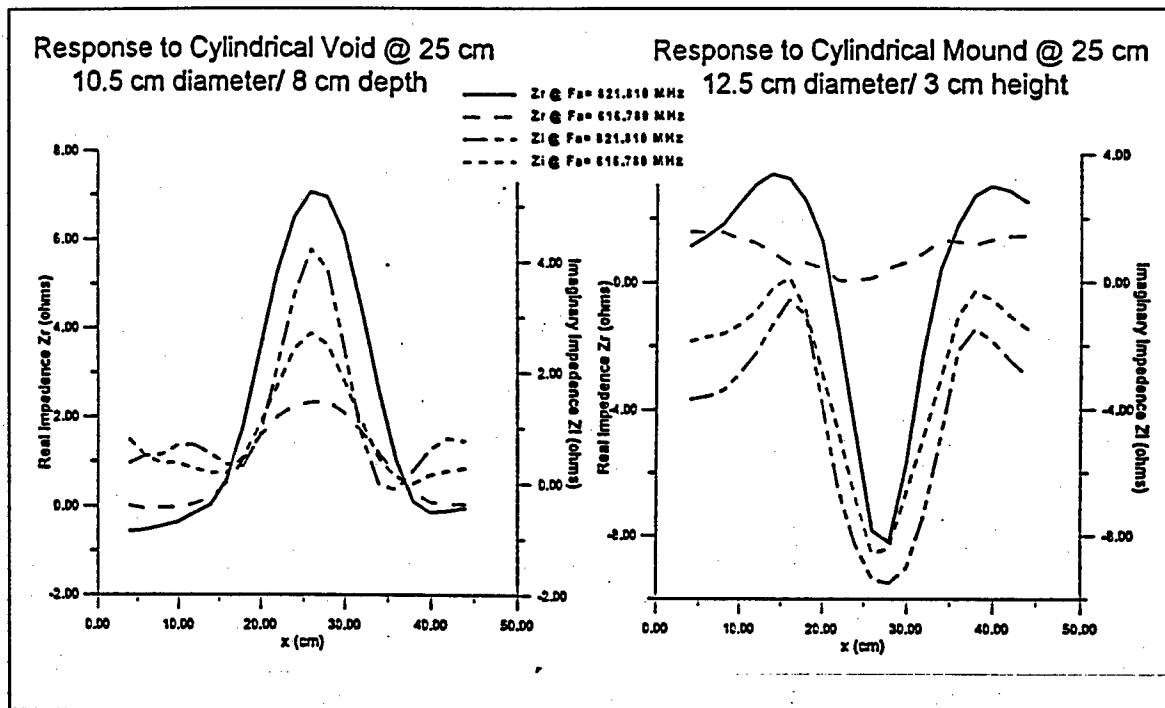


Figure 29: RMPA impedance response to a soil void and surface mound using the 821/616 MHz frequency, 10.2 di-electric dual feed-point patch..

We do not yet have field data from the RF circuitry. However, data specifically recorded by the EDIT electronics will be available after lab testing in the middle of April. Correlation between HP soil tests and EDIT detector field tests are the focus of our local field tests to be conducted in April at an outdoor test lane site in Raton. RMPA data recorded at RTR are continuously being sent to LANL for algorithm design for the height correction processing. Detailed analysis of the algorithm efficiency will continue and the refined structure will be moved to the 386 platform of the Elan SC300 microprocessor in February. The theoretical response of the antenna to height variations as predicted by the correcting algorithm is still well correlated to the laboratory experimental antenna tests.

An analytic representation of the electrodynamics of RMPA landmine detection has been developed to the extent that it shows good qualitative agreement with laboratory tests. This representation uses an approximation to the 3-D standing waves established between the patch antenna, the air-earth interface, and the landmine. This work has elucidated features of detector operation that are incorporated into a mathematical algorithm to convert detector impedance characteristics into recognizable indicators of land mine presence. The previously discussed RTR data is in good agreement with the analytic representation. Work is currently underway to adapt the detection algorithm to the specific characteristics of the hardware and adapt the system to the wide range of field conditions anticipated.



4. EDIT Land Mine Detector

4.1 EDIT System Description

The EDIT Detector development, as described in the previous Phase 1 Monthly Reports, has produced an instrument design that is entirely self contained, portable, ergonomic, and low maintenance. The goal of the development was to create an affordable and sustainable instrument designed to collapse and fold up on itself for easy transport with a minimum of steps and does not require external connector attachments. The design also incorporates a more ambidextrous versatility that allows an out-of-the-box operating capability with no in-field modification of the assembled instrument. Besides the ergonomic design features, the instrument produces silhouette images to assist in identification of the buried source object. The EDIT detector's mechanical design includes three main sections:

- Sensor Head with Positioning System
- User Interface with RF Modem
- Power Center with Battery Monitor

4.1.1. Sensor Head

The sensor head consists of a 10-inch diameter acrylic composite chamber containing the RF circuits, metal detector, x-y positioning transmitter, and RMPA antenna. The sensor head, as seen in Figure 30, is connected to the lower chassis shaft at a cylindrical swivel joint. The tension screw at this joint allows adjustable positioning angles to the telescopic lower shaft. The wiring connector for the sensor head protrudes from the lower shaft just above the swivel joint and attaches to the head with a ratcheting mil-spec connector. The acrylic sensor head skeleton is capped by 0.25" removable upper and lower Lexan plates and covered by a 0.0625" Lexan shell. The 0.125" thick lower plate contains housing for the RMPA antenna. The upper plate possesses the standoff mounts for the electronics as well as the lower shaft attachment joint and sensor cable connector. The assembled weight of the sensor head is presently 2.9 lbs. and plans for a more lightweight injection molded enclosure are pending.

The electronics assembly consists of the RF board, CFS/D board, digital interface board, and the microprocessor board. These 4 circuit boards, connected via PC-104 standard bus, and mounted to the upper head plate extend down 3 inches from the upper mounts and 1 inch up from the antenna. Sufficient space has been left to accommodate the LANL positioning subsystem whose antenna should be located on the sensor head directly above the resonant patch center-point.



RATON
TECHNOLOGY
RESEARCH

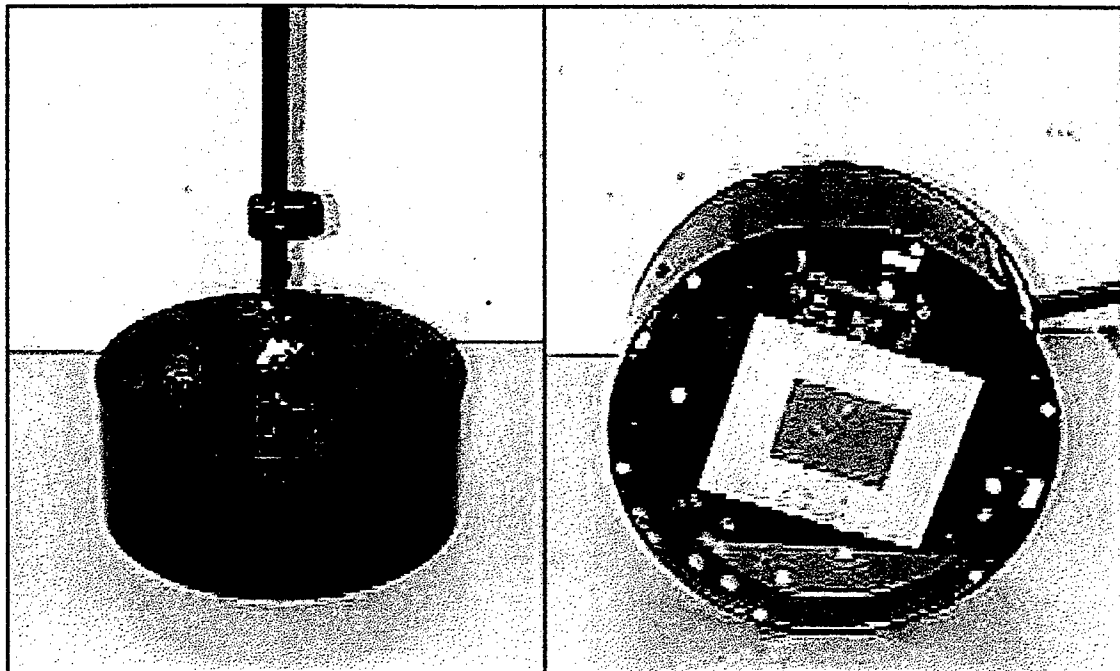


Figure 30: Photographs of the EDIT Land Mine Detector Sensor Head built for prototype testing of the hand-held unit.

4.1.2. User Interface

The user interface is the entire front section of upper chassis consisting of a handgrip with trigger switch, master microprocessor, and visual display. The display unit resides within a protected enclosure attached to the top of the handgrip forming a weatherproof enclosure. The user interface functionality is ambidextrous in nature and allows the instrument to be operated via the soft keypads and recording switch accessible with the gripping hand. The soft keys on the display unit are just above the handgrip within reach of the user's thumb. The data record switch exits the front of the handgrip where it is easily toggled like a forefinger trigger. These functions are fluidly operated by either the left or right hand, while maintaining control of the sensor head with the handgrip. The data transmission modem is currently attached to the front of the display housing. An internal speaker provides audio tones based on the detection of subsurface objects.

The cabling has been completed for the display, which is now capable of showing characters on the Seiko G321EX model. The G321EX requires 4 bit data, which is compatible with the Elam SC300 controller, which drives 4 bits of pixel data at a time. The gray scale/ color



requires 2 bits per pixel. The display resolution is a 320 x 240 pixel system with 1 bit per pixel and will have a refresh rate of either 57.4 or 86.1 Hz depending on the undecided CGA/HGA display modes. In addition, the display housing drawings are being reviewed for subsequent construction and assembly. Work also continues on specific messages exchanged by sub-modules in the system, and on the internal control of the LCD by the Elan SC300 microcontroller. Figure 31 is a photograph of the operational display screen.

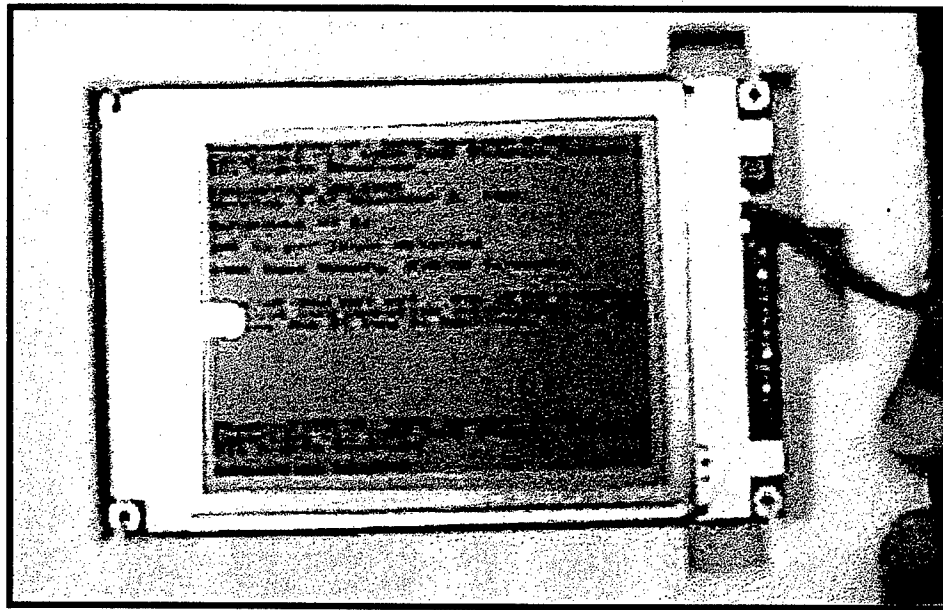


Figure 31: Photograph of the newly operational Seiko G321EX display screen.

Figure 32 diagrams the intended layout of the user interface display, including view screen, operational indicators, and soft key pad. The operational indicator screens below the main display will lead the user through the 4 main steps of operation: power-up and self tests, instrument calibration, homing of x-y position system, and recording of field data.

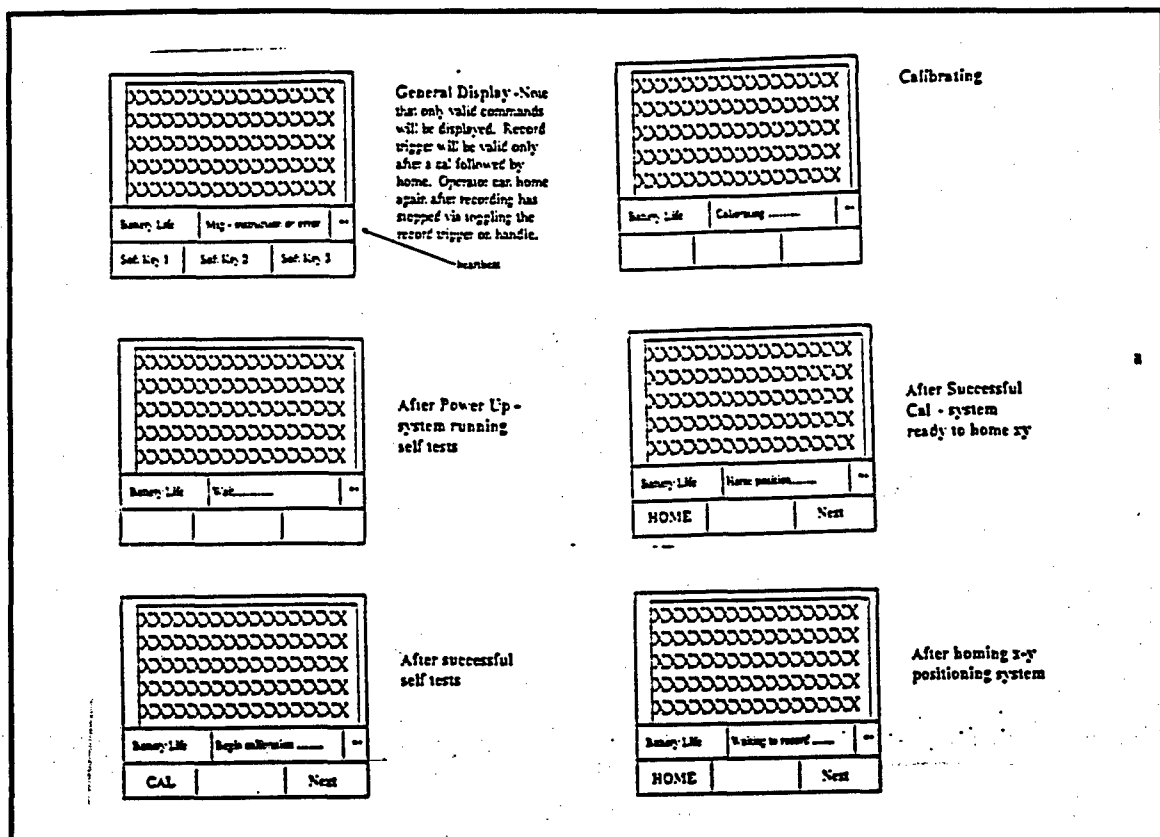


Figure 32: Diagrams of the user interface display showing the potential order of operation. This procedure will include system tests, sensor calibration, home positioning, and finally the recording of field measurements.

4.1.3. Power Management

The Power Center enclosure at the rear section of upper chassis contains the two D-cell battery packs. The battery pack design allows the insertion of 8 D-cells in series to be loaded from the rear of the pack in a procedure similar to loading a flashlight. The power center enclosure is a permanent extension of the upper chassis and serves as the counter-balance weight to the assembly. The Power Center, seen in Figure 33, performs both battery monitoring and battery charging. Battery charging is accomplished by an external 9-volt AC adapter or 24-volt DC solar panel, either of which can be attached to a jack in the rear of the module. For more advanced power monitoring during this development phase, the Power Center also contains a 9-pin serial port, LCD display, and keypad. A warning speaker



indicates a low battery level and an external switch controls power to the rest of the instrument and is externally fused.

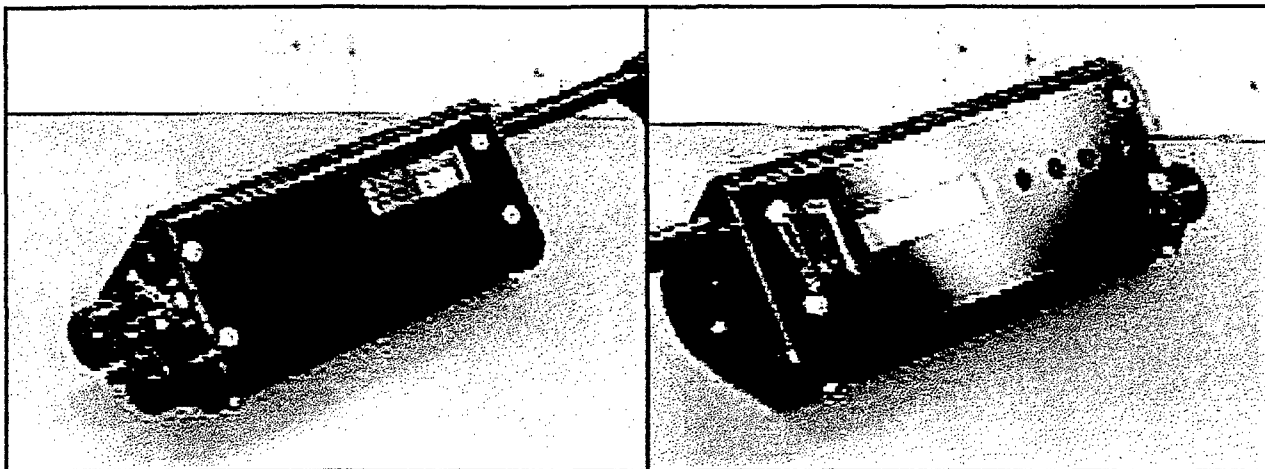


Figure 33: Advanced Power Center containing microcomputer controlled battery monitoring circuitry, charging jacks, 9-pin serial port, power warning speaker, and external fuse jack.

The Power Center is compatible with all the following battery chemistries: NiCd, NiMH, Sealed Lead Acid, Rechargeable Alkaline Manganese, Li-Ion, and Li-Polymer. During field testing standard Alkaline D-cells will be used.

Power management involves two different systems; battery monitoring and power regulation. Internal voltage regulation will be done by individual subsystems using the power bus lines. The sensor head electronics have 3 +5Vdc (5Watt) step up switchers (MAX608 designs) and 1 -5Vdc inverter (MAX774) attached to one of the 3 +5Vdc switchers. Two of the three MAX608 switchers are assigned and so is the -5Vdc inverter. The remaining +5Vdc 5Watt switcher is available for the xy-positioner or it can use the unregulated battery supply. Both of these available outputs are connectorized using the Molex type or Berg type .100" spacing right angle posts. Also, the RS485 lines from the Embedded PC104 are also available on this same connector.



4.2 EDIT Mechanical and Software Design

4.2.1. Prototype Assembly

The assembled detector prototype, with resonant microstrip patch antenna (RMPA), graphical user interface, and 8 D-cell batteries installed weighs just over 18 lbs. The block diagram of the EDIT Land Mine Detector is shown in Figure 34.

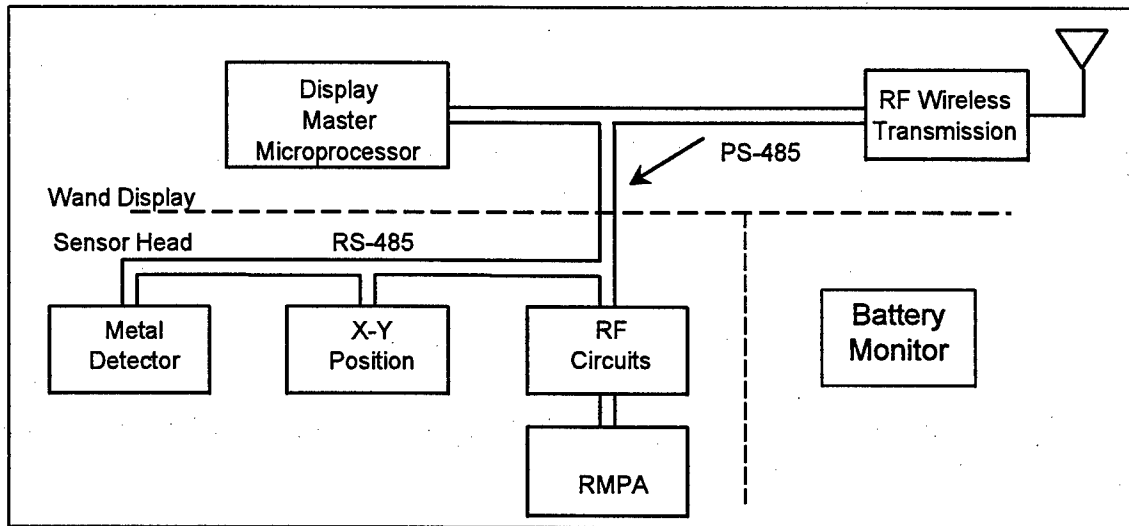


Figure 34: Block diagram of EDIT Land Mine Detector sub-systems.

The mechanical design of the EDIT detector includes telescoping tube sections between the User Interface and the Battery Pack (designated "Upper Chassis") and between the User Interface and the Sensor Head (designated "Lower Chassis"). At present, each tube chassis is constructed of aluminum sections containing retractile cables, which allow for extending or retracting the over-all instrument length. This should allow the user to comfortably modify the "fit" of the unit for operation.

An operational prototype detector is currently being assembled at RTR and includes only the sensor head, chassis, and power center. The user interface has been built by LANL and is currently being integrated into the instrument. The EDIT Land Mine Detector's current mechanical design is rugged, low maintenance, and weather resistant. This portable field instrument, shown in Figure 35, is designed to collapse and fold in on it self for easy transport and storage with a minimum of steps, and is entirely self contained, requiring no external connectors.



Figure 35: Series of photos showing the deployment procedure for the EDIT detector.

4.2.2. Chassis and Cable System

The lower chassis is attached to the upper chassis at a fully adjustable swivel mount directly behind the handgrip. The handgrip position is controlled by a ball and socket swivel joint allowing complete adjustment by the user. The upper and lower shafts contain pigtail cable within their inner diameter through which 8-conductor wire harness travels from the display to the sensor head, and back to the power center. The upper shaft also has 3-section telescopic ability to allow lever arm extension for the counter-balance weight adjustment.

The connectors are of the MIL-C-38999 series III type, and consist of an 11-shell size, 0.750-diameter thread, and 5-pin connector shell with a 11-5 insert. Pins are 20 contact size, rated at 7.5 amperes. The connector was changed from 8-pin to 5-pin, allowing the minimum number of cable conductors to be used (2 for RS-485; 2 for Battery + and -; and one spare), and works out fine for the 5-conductor retractile cable chosen for each chassis. The cable requirements



result from the fact that the chassis segments shall remain as lightweight as possible, but extend out to 4 feet, if possible.

A 5-conductor retractile communication cable with polypropylene insulation (0.012") and a PVC jacket was chosen. The cable has an operating temperature range of -20 degrees C to 80 degrees C, and a voltage rating of 300 Volts at 1 Ampere. The cable-retracted length is 1 ft., extended length of 5 ft., and has 12-inch leads. Readily available tube sections were taken from "Bogen/Manfrotto" camera tripods and modified for a new demo unit. The revised cabling will use 5-conductor mil connectors as shown in Figure 36.

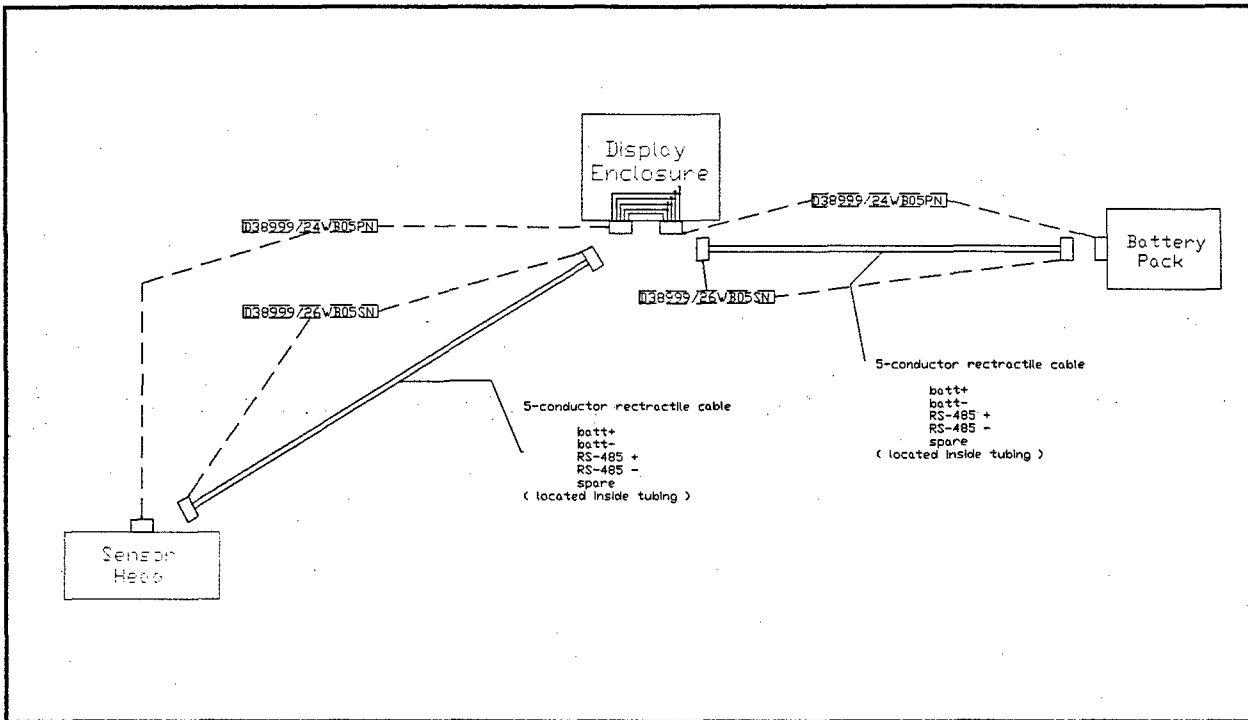


Figure 36: Schematic of EDIT wire harness and connector design and module conductor assignments.

Also, it was determined that each sub-system is to provide its own power regulation. Separate regulators will be designed into the display unit and the Sensor Head electronic package. (Regulator circuits are already developed for the Head computer, RF and CFS/D boards and a regulator for the X-Y transmitter).

Please also note that the connector wiring is shown so that the minimum number of connector pins are used, keeping in mind that this could eventually change to a three-connector wiring harness 'down the road' (which will be more manufacturable for volume production). This cabling scheme also maintains a spare line if needed, since a 5-conductor connector is standard.

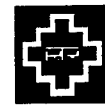


RATON
TECHNOLOGY
RESEARCH

4.2.3 System Software

The control software for the measurement instrumentation has been completed and tested with the new Power/Input/Output Interface board. The RTR control program will act as a slave component to the master control program being run on the User Interface processor. The RTR program makes continuous measurements when enabled and reports the immediately previous measurement data upon command from the master program. An auxiliary master program for testing the RTR control software has also been completed and will be used for testing / data collection until the Los Alamos master program is available.

The RTR control software is written in Watcom C and runs under the QNX real-time operating system. The control program will be run on a MSM386 microcomputer from Advanced Digital Logic. This microcomputer has a PC104 form factor with the standard PC104 connections and will be positioned near the top of the measurement instrumentation board "stack". Besides performing the control functions required by the instrument, this microcomputer contains a RS485 interface and provides communication with the User Interface master microcomputer.



5. Positioning Systems

The positioning system is a key component in the multiple-sensor mine detection system. The same positioning system will also be used by the RMPA detector which will provide a common mine field coordinate system for all three detector or sensor systems during the landmine detection. In the detection process, the RMPA system will scan the field first and a coarse grain mine field map will be generated in real time. After detecting and marking possible mine objects, the LMR system will image the suspected areas marked by RMPA with the common positioning system confirming the location. There are at least two options for the positioning system; one is an RF x-y positioning system which uses microwave and its phase information to measure the location and the other is a two dimensional sonic x-y digitizer system that uses sonic technology to measure and digitize location.

5.1 RF X-Y Positioning System

The fundamental configuration of the RF x-y positioning system is three receivers and one transmitter. The transmitter will be located at a fixed position on the LMR vehicle and the three receivers are located along a reference base line behind the survey area. After RMPA scans the area, the scanned area will be digitized and stored in the computer and suspected objects will be marked on the field and highlighted in the digital map. As the LMR system approaches these areas, the RF x-y positioning system will sample the location of LMR system continuously. When the x-ray tube head is at a suitable location for imaging the suspected object, the vehicle stops and the LMR system starts to image the area which is suitable to cover the suspected object.

5.1.1 Description of EDIT Detector X-Y Positioning System

The configuration of the positioning antennas during a survey composed of 1 meter square sections is diagrammed in the Figure 37.

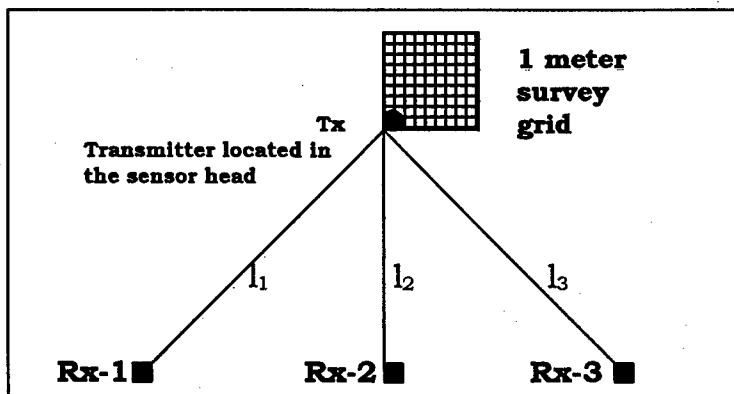


Figure 37: Configuration of Receiver Antenna Base Line with 10 meter Separation during field survey.



The vertically polarized transmitting antenna is located in the sensor head of the EDIT detector with the RMPA antenna. The companion receiver antennas are located along a reference base line behind the survey area and operator. The basic theory of the positioning system relies on the measurement of the 50 MHz signal phase shift with changing travel path length between the Tx and Rx units. The X-Y Positioning System Block Diagram is illustrated in the Figure 38.

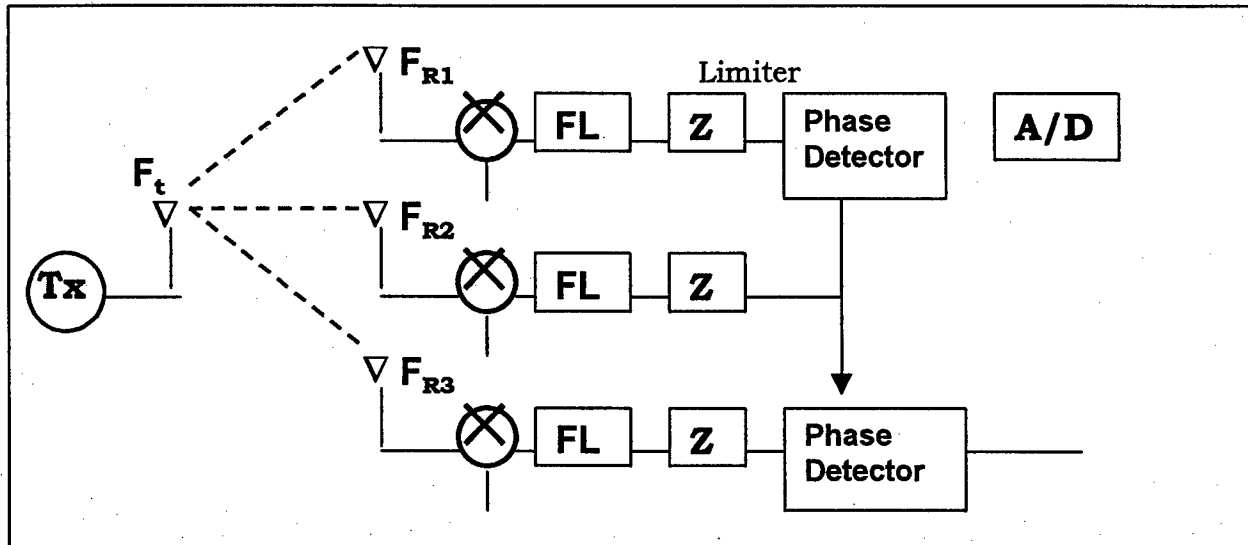


Figure 38: Block Diagram of X-Y Positioning System's phase sensitive electronics.

This phase shift is defined by a system of equations relating the transmitted frequency, the local oscillating frequency, and the received mixed and filtered frequencies.

Transmitted Frequency is defined as:
 $F_t = A \sin(\omega_0 t + \theta_0)$

Where $\omega_0 = 2 \pi F_0$
 $F_0 = \text{operating frequency in Hz} \quad (50\text{e}6 \text{ Hz})$
 $\theta_0 = \text{initial phase shift}$

The local oscillator frequency is F_{lo} and is set such that $F_0 - F_{lo} = F_{if}$

The Received Frequencies are defined as:

$$\begin{aligned} F_{R1} &= AB \sin(\omega_0 t + \theta_0 + (360/\lambda) l_1) \\ F_{R2} &= AB \sin(\omega_0 t + \theta_0 + (360/\lambda) l_2) \\ F_{R3} &= AB \sin(\omega_0 t + \theta_0 + (360/\lambda) l_3) \end{aligned}$$



However, the filtered frequencies after the mixers are defined as:

$$F_{R1m} = ABC \sin (\omega_{IF} t + [\theta_0 - \theta_{lo} + \theta_1] + (360/\lambda) l_1)$$

$$F_{R2m} = ABC \sin (\omega_{IF} t + [\theta_0 - \theta_{lo} + \theta_2] + (360/\lambda) l_2)$$

$$F_{R3m} = ABC \sin (\omega_{IF} t + [\theta_0 - \theta_{lo} + \theta_3] + (360/\lambda) l_3)$$

The signal is limited prior to phase detection. A switching type phase detector effectively mixes the signal.

However, the filtered frequencies after the mixers are defined as:

$$F_{DU} = D \sin ([\theta_1 - \theta_2] + (360/\lambda) [l_1 - l_2])$$

$$F_{DL} = D \sin ([\theta_2 - \theta_3] + (360/\lambda) [l_2 - l_3])$$

Thus, during a survey, the three measured phase shifts will provide a spatial coordinate relative to the base-line array distance. These coordinates will be attached to RMPA impedance values at 1-cm intervals within the survey grid.

5.1.2 Positioning System Instrumentation

The deliverable version of the x-y positioning system is currently being built by LANL. The design has been modified to make the sensor head lighter and the positioning system more robust. Initially, three receivers, each at a different frequency, were to be placed in the sensor head, while the transmitter was in a fixed position in a small base station located behind the test lanes. Now, three receivers will be housed in the base station, and one transmitter at a single frequency will be located on the sensor head. This configuration is more deterministic than the original solution, and yields a more unique and simpler transfer function as well. Laboratory tests have verified that the new design meets all system specifications and requirements. The RF modems are now able to communicate x-y data.

5.2 Sonic X-Y Positioning System

The sonic x-y positioning system has a sonic impulse generator and a receiver and a processing system. A commercial product designed for digitizing maps can be used in place of the RF X-Y Location system for a self-contained demining positioner. The sonic impulses which are generated continuously by the impulse generator are received by the receiver and



RATON
TECHNOLOGY
RESEARCH

the distance between these two is calculated and processed and stored in the computer. Similar to the RF system described above, the sonic impulse generator will be located at fixed position on the EDIT Sensor Head, the distance will be continuously determined. Due to restrictions of this positioning system, the effective real-time maximum scanning area is 100 cm by 150 cm. In field operations the sonic receiver would be placed at the start line of the lane being surveyed. The sonic data would then be transmitted from the sonic receiver by RS-232 wireline or by a RF modem.



6. Nuclear Quadripole Resonance (NQR)

It is believed that using synchronous detection where the receiver noise bandwidth is minimized can enhance detection sensitivity. Therefore, experts in nuclear physics and electrical engineering are currently assessing the direct combination of the associated hardware of RMPA and NQR. The NQR signal is an oscillating magnetic field, while the resonant antenna is designed to create strong electric coupling, however much of the requisite electronics for both systems are very similar.

In an investigation by S.K. Lamoreaux of LANL Physics Division, the applicability of NQR to mine detection was discussed. As reported in the Appended Technical Report, Lamoreaux concludes that the ferrite bar magnet has a net signal increase of a factor of 10 over a pick-up coil for measuring induced voltage for NQR detection of RDX. The report also states that a SQUID magnetometer may be the most promising sensor based on its increased magnetic sensitivity. However, NQR is described as being limited to a small class of explosive crystalline structures with large quadrupole precession frequencies.



7. SYSTEM RELATIONSHIP

In the proposed multiple-sensor detection system, the relationship between the lateral migration radiography (LMR) system and resonant microstrip patch antenna (RMPA) system will be as follows:

- Several hand-held EDIT Detectors will be used to search an area for buried or surface mine-like objects. Whenever a suspect image is produced, that location will be marked with a color-code representing the suspected object size category.
- The LMR system, which will be guided by the same RF or sonic x-y positioning system used by RMPA, will scan the marked site to obtain LMR images of suspected objects. After image processing and application of target recognition algorithms, the objects will be identified as mines or non-mine objects.
- For mines, information will be provided on the type, shape, x-y location and depth-of-burial.

7.1 System Integration

Work not started. Phase II document proposing system integration is pending.



RATON
TECHNOLOGY
RESEARCH

Appendix

Overview of Nuclear Quadrupole Resonance Based Mine Detection

Small Business Technology Transfer (STTR) Solicitation Topic 97T006
Multi-Sensor Detection, Imaging, and Explosive Confirmation of Mines

Monthly Report No. 6
RTR-98-010

Page 55

S.K. Lamoreaux, Los Alamos National Laboratory
 Physics Division, P-23
 Neutron Science and Technology, M.S. H803
 Los Alamos, NM 87545

Feb. 17, 1998

I. OVERVIEW OF NUCLEAR QUADRUPOLE RESONANCE BASED MINE DETECTION

A. Report Contents

In this review, I give an overview of expected signal strengths and efficacy of various detection methods in the application of Nuclear Quadrupole Resonance (NQR) to detect explosives; the primary motivation is for the remote detection of anti-personnel land-mines, but this technology might have application to, for example, airport security. This report will be focussed toward land-mine detection.

In Sec. IB, an estimate of the signal strength for the "ideal" explosive RDX will be given. In Sec. II, the physics of magnetic flux collection by a ferrite rod is developed, and it is shown that use of such offers a number of advantages in regard to detection of the NQR magnetization signal. In Sec. III, the effects of shielding by conductors is considered. Sec. IV gives an analysis of the applicability of SQUID detection to this problem. In Sec. V, possible application to other explosive materials is considered, and what material properties are important for reliable detection by NQR. In Sec. VI, the conclusions of my study are presented.

B. Signal Strength

NQR based mine detection is based on the observation of a specific magnetization precession signal associated with a coupling of the ^{14}N nuclear quadrupole moment with a local crystal field.

Under equilibrium conditions, the ^{14}N nuclear quadrupole moment will become aligned in the local microscopic electric field at each lattice site in a crystalline material. If the quadrupole moment orientation is subjected to a radiofrequency magnetic spin flip pulse, the net orientation will be transformed to a precessing magnetization; the associated frequencies are a specific signature of a given material.

Abragam (Ref. 1, p. 259 ff) estimates the magnetization signal as a function of time for a single perfect crystal, when the orientation axis is along \hat{z} :

$$M_z(t) = \frac{N\gamma\hbar^2\omega_0}{(2I+1)kT} \alpha \sin(\alpha\gamma H_1 t_w) \sin(\omega_0 t) \quad (1)$$

where N is the volume density of the nucleus of interest, γ is the gyromagnetic ratio (rad/s/G), ω_0 is the quadrupole resonance precession frequency (rad/s), I is the nuclear spin, α is a constant of order unity, H_1 is the radiofrequency magnetic field strength, and t_w is the RF pulse width; this formula assumes that t_w is much less than the relaxation time. k is Boltzmann's factor, and T is the sample temperature.

The precession signal is in phase with the RF pulse, and is directed along the RF pulse axis \hat{z} .

Taking as an example 100 g of the explosive RDX, we find, with the following parameters (density 1.5 g/cc, 38% ^{14}N):

$$\omega_0 = 2\pi(5 \text{ MHz})$$

$$N = 2.45 \times 10^{28} / \text{m}^3$$

$$\gamma = 2\pi(3.076 \text{ MHz/T})$$

$$\alpha \approx 1$$

$$T = 300 \text{ K.}$$

and taking t_w such that the sin term is about unity, that the precessing magnetization has amplitude

$$M_z = 1.33 \times 10^{-5} \text{ J}/(\text{T m}^3). \quad (2)$$

This assumes a perfect crystalline material, in which case the precessing magnetization is homogeneous throughout the sample.

If the sample is in the form of a sphere, the magnetic induction as a function of position along the x axis is given by (See Ref. 2, p. 197)

$$B_z = \mu_0 M_z \frac{V}{r^3} \quad (3)$$

where $\mu_0 = 4\pi \times 10^{-7}$ and V is the sample volume in m^3 . For a 100 g sample, the field 20 cm away is thus

$$B_z = 1.4 \times 10^{-14} \text{ T.} \quad (4)$$

For direct electrical pickup, assume a 10 turn coil, 10 cm diameter, tuned to resonance, and $Q = 20$. The voltage induced on this coil by the oscillating magnetic field is given by (assuming a constant magnetic field across the coil)

$$V = Q\omega_0 n A B_z = 0.7 \mu\text{V} \quad (5)$$

where n is the number of turns and A is the coil cross sectional area. However, in this estimate, we have assumed that the sample is in the form of a perfect crystal. In fact, for a typical polycrystalline material, we must

average over all possible crystal axis angles, and such averaging will reduce the above estimate by a factor of about 6. Note that increasing the pickup coil diameter will not give rise to a larger signal; this is because the Q diminishes for a larger diameter, and the variation in B_z across the diameter must be taken into account. Also, the maximum n is limited because of self-resonance of the coil.

Thus, in order to detect a 100 g sample of RDX at 20 cm distance from a 10 cm diameter pickup coil, we must be able to detect a $0.1 \mu\text{V}$ signal with a S/N of about 5 in about a 1 kHz bandwidth; this is a difficult problem.

II. FLUX COLLECTION INTO A FERRITE ROD

Use of a ferrite bar coil antenna can significantly increase the detected signal by increasing the effective diameter of a pickup coil; a ferrite rod of length ℓ will collect flux out to a radius of order ℓ^2 , with only a small effect due to the rod diameter $2R$. Therefore, n can be increased; in addition, Q remains high. The effective flux suck-in area can be estimated as follows.

Working in cylindrical coordinates, we assume the rod center is at $z = 0$, $\rho = 0$. The ends are at $z = \pm \ell/2$. Assuming a simple model of the effective surface pole density that gives rise to the "magnetic potential" within the rod, by requiring that the internal magnetic field is zero (true for a high permeability material) due to the cancellation of the external field by the surface pole density, the magnetic induction within the rod can be determined.

Assume a surface pole density of
a) on ends,

$$\sigma(\rho) = \text{const} = \sigma_0 \quad (6)$$

b) along length

$$\sigma(z) = 2\alpha\sigma_0 z/\ell \quad (7)$$

where α is a constant to be experimentally determined.

The magnetic field is given by

$$\vec{H}(\vec{z}) = -\vec{\nabla}\phi(\vec{z}) \quad (8)$$

where

$$\phi(\vec{z}) = \frac{1}{4\pi} \int_S \frac{\sigma(\vec{z}')}{|\vec{z} - \vec{z}'|} dS. \quad (9)$$

The potential at the center of each rod end, due to the pole distribution on both ends, is

$$\phi_e = \pm \frac{1}{2} \int_0^R \left(1 - \frac{\rho}{\sqrt{\rho^2 + \ell^2}} \right) \sigma_0 d\rho \quad (10)$$

which in the limit $a = \ell/R \gg 1$ gives

$$\phi_e = \pm \frac{\sigma_0 R}{2} \left(1 - \sqrt{1 + a^2} + a \right). \quad (11)$$

The potential at the center of either end, due to the pole distribution along the rod length is

$$\phi_s = \int_{\ell/2}^{\ell/2} \frac{R}{\sqrt{R^2 + (z \pm \ell/2)^2}} \frac{\alpha\sigma_0 z}{\ell} dz \quad (12)$$

which can be integrated to yield

$$\phi_s = \pm \alpha\sigma_0 R \left[a^{-1} - \sqrt{1 + a^{-2}} + \frac{1}{2} \ln(\sqrt{1 + a^2} + a) \right]. \quad (13)$$

The difference in the total potential on either end, divided by the separation between the ends ℓ is equal to the magnetic field at the center:

$$H_c = \frac{\Delta\phi_{\text{tot}}}{\ell} = \frac{2(\phi_e + \phi_s)}{\ell} = \sigma_0 K/a \quad (14)$$

where

$$K = 1 - \sqrt{1 + a^2} + a$$

$$+ a \left[\ln(\sqrt{1 + a^2} + a) + 2a^{-1} - 2\sqrt{1 + a^{-2}} \right]. \quad (15)$$

The constant σ_0 is determined by the requirement that for a high permeability material ($\mu \rightarrow \infty$), the internal field H_c due to the surface pole distribution must cancel the initial external field H_0 (no net H field within the rod); this implies that

$$\sigma_0 K/a = H_0$$

which determines σ_0 .

Next, for a high permeability material, the field must enter normal to the surface. This implies that every surface pole gives rise to a unit of flux. The net internal magnetic field, as a function of z along the length of the rod, is given by the integral of the surface pole distribution up to that point:

$$\Phi_m(z) = \mu_0 \left[\int_0^z 2\pi R \sigma_0 \rho d\rho + \int_z^{\ell/2} 2\pi R \sigma(z') dz' \right] \quad (16)$$

or, at the center of the rod,

$$\Phi_m = \mu_0 \left(\sigma_0 \pi R^2 + 2\pi R \frac{\alpha\sigma_0 \ell}{4} \right) = \mu_0 \sigma_0 \pi R^2 (1 + \alpha a/2). \quad (17)$$

Taking the ratio of the magnetic flux through a loop equal in diameter to that of the rod, with and without the rod in place, gives

$$\kappa = \frac{\Phi_m}{\Phi_0} = \frac{a}{K} (1 + \alpha a/2) \quad (18)$$

which can be thought of as the flux collection factor. The relative error of this formula is approximately $1/\mu$, so for $\mu > 10$ the error is less than 10%.

Experimental measurements on a rod of diameter 1.3 cm and length 15.8 cm, with permeability $\mu = 55$, indicates that $\alpha = 2.0 \pm .01$ (found by measuring $\Phi_m(z)$). The experimentally measured $\kappa = 130 \pm 10$ which compares well with $\kappa = 120$ from the above theory.

In regard to NQR detection, even though the cross sectional area A is smaller when a ferrite rod is used, the effective diameter is approximately equal to the length of the rod. In addition, with a ferrite bar n can be increased, as well as Q ; the net gain in flux collection and induced voltage can be of order a factor of 10 greater than for a bare coil, bringing the above voltage estimate to about 1 μ V which is a more reasonable signal.

A. Additional Inductance of a Loop when placed over an Infinitely Long Rod of Permeability μ

This problem is solved in Smythe (Ref. 2), p. 324, Problem 15. We are considering rods with $\ell/R \gg 1$ so the infinite length approximation is reasonable.

From Ref. 2, in the case where the coil is wound directly onto the ferrite rod, the change in inductance is given by

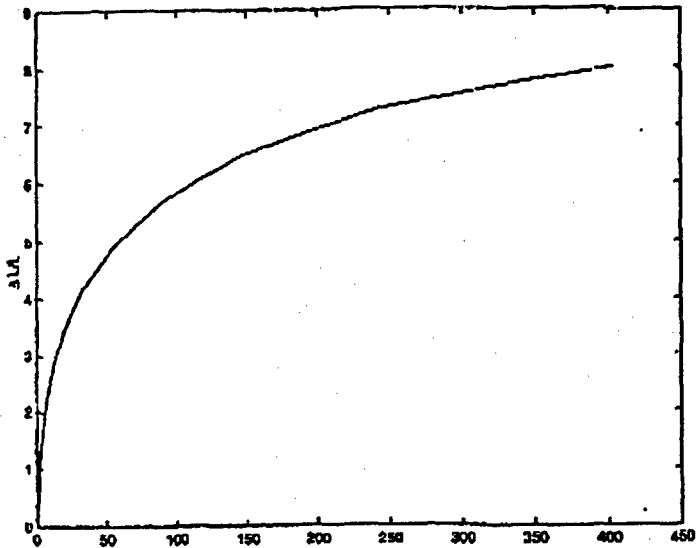
$$\Delta L = 2\mu_0 R \int_0^\infty \frac{(\mu - 1)x I_0(x) I_1(x) [K_1(x)]^2}{(\mu - 1)x K_0(x) I_1(x) + 1} dx \quad (19)$$

while the inductance of a circular loop wound with wire of radius b , in free space, is (assuming the high frequency limit)

$$L = \mu_0 R [\ln(8R/b) - 2] \quad (20)$$

(for n closely spaced turns, the inductance increases by a factor n^2).

Taking $R/b \approx 20$, $\Delta L/L$ can be readily calculated as a function of μ . A plot is attached below.



We immediately see the advantage to use of a ferrite rod to collect the flux; the rod length can be made very large, thereby increasing the effective cross sectional area, while not unduly increasing the coil inductance. The smaller cross sectional area means that a greater number of turns can be added. Taking the case of a 30 cm long ferrite bar, 1 cm diameter, with $\mu = 100$, we find $\kappa = 300$. This implies that for a coil to give the same response, without a ferrite rod and with the same number of turns, would have to have a diameter of 17 cm, and the inductance would be 26 times that of a 1 cm diameter coil without the ferrite bar; from the above plot, the effect of the rod would be to increase the inductance by a factor of 6; this means that n could be increased by a factor of over two for the ferrite bar, while maintaining the same inductance as a free space coil. Furthermore, the self resonant frequency of the ferrite bar is much higher due to the lower distributed capacitance, and the resistive loss is lower due to the reduced total wire length in the coil; these factors together can lead to an order of magnitude increase in effective signal detection for a ferrite rod antenna system, as mentioned before, due primarily to the net increase in Q and n .

III. SHIELDING DUE TO METAL FOILS OR CONDUCTIVE SOIL

There are two effects of shielding of the oscillating field by conductive materials. First, we consider the case where we have set the RF spin flip pulse width to give a maximum signal as indicated in Eq. (1) without conductors. If we parameterize the reduction in magnetic signal strength by a multiplicative factor β , for $\beta \ll 1$, the sin term in (1) becomes linear in β .

Second, the magnetization precession signal will be reduced by a factor of β also; together with the reduction in

pulse width, the net signal reduction, in the case $\beta \ll 1$, becomes proportional to β^2 .

The coil used to generate the spin flip RF pulse should be a pancake coil with diameter much greater than the expected maximum mine depth. If the diameter of the coil is made equal to the maximum expected mine depth, the reduction in signal strength due to a non-optimally tuned RF pulse due to distance variations will be minimized.

The shielding effects for various materials can be easily estimated; the skin depth for a material of conductivity σ for a magnetic field of frequency f is given by

$$\text{Skin depth, cm} = \frac{1}{2\pi} \sqrt{\frac{10^9 \mu}{\mu f}} = 5,033 \sqrt{\frac{\mu}{\mu f}} \quad (21)$$

where μ is the magnetic permeability of the material, and ρ is the volume resistivity in ohm-cm. For copper, the skin depth is $6.62/\sqrt{f}$ cm; for 5 MHz, this thickness is 0.001 inch. Since the resistivity enters as a square root, most pure metals will be within a factor of 5 of this value.

The resistivity of moist ground is about 1-10 k Ω cm; so the penetration depth is over 1 m in most instances.

The main concern is metallic components or foil used in the land-mine; this could either shield or distort the RF pulse or magnetization signal. An engineering study of this point is needed.

IV. SQUID DETECTION OF NQR SIGNAL

The use of a (cryogenic) ferrite rod with a superconducting flux pickup coil coupled into a SQUID offers a number of attractive features. First, as mentioned before, the effective cross sectional area of the pickup loop can be made arbitrarily large without unduly increasing the loop inductance; this point is particularly important for a coupled SQUID system. Second, the cryogenic system can be relatively compact with the smaller diameter loop.

For a 1 cm diameter coil wound on a ferrite bar with $\mu = 100$, with wire diameter 0.030 inches, the inductance is 100 nH (where the correction described in Sec. II A is included); the flux coupled into this coil is given by Eq. (4) (divided by 6 for the polycrystalline material) and Eq. (18) (for a 30 cm long 1 cm diameter rod, $\kappa = 300$), giving

$$\Phi_m = 5.5 \times 10^{-17} \text{ Tm}^2$$

leading to a pickup coil current of

$$\Phi_m/L_p = I_p = 0.5 \text{ nA.}$$

This is a relatively large current; assuming the input coil inductance of the SQUID L_i is much lower than L_p , the flux coupled into the SQUID is given by the input mutual

inductance M times this current. A typical value is $M = 10 \text{ nH}$ giving an input flux of $5 \times 10^{-18} \text{ Tm}^2$ which is 2.4×10^{-3} flux quanta (Φ_0).

The energy resolution of a SQUID is given in units of \hbar , with a 1h SQUID having a flux measurement noise of $0.1\mu\Phi_0/\sqrt{\text{Hz}}$. If we take a 10 KHz bandwidth for our system, the 1h noise would be $10 \mu\Phi_0$. The above signal estimate can be used to calculate the intrinsic energy resolution required:

$$N_h \approx (2.4 \times 10^{-3}/10 \times 10^{-6})^2 = 5.76 \times 10^4$$

so we need a $50,000\text{h}$ SQUID to achieve a S/N of unity in a 10 KHz bandwidth. If we require a S/N on the flux detection of 10, then a 500h SQUID is required; the intrinsic resolution of an off-the-shelf Conductus 1020 is 900h which would be good enough for this application.

An important question is whether the SQUID will be overwhelmed by external electrical noise sources, both natural and man-made. The NQR pickup system could be enclosed in a metal box with the bottom open; this would shield noise from above ground. Also, the ferrite bar could be bent in a horseshoe, thereby giving a differential measurement along the ground.

A practical scheme might be to have a low-frequency feedback system, keeping the flux on average zero in the ferrite bar. The high frequency signal could then be picked up directly from the SQUID.

The SQUID has an advantage over the direct electrical pickup case in that the sensitivity is linear in the NQR frequency ω_0 ; for the direct pickup, there are two factors of ω_0 , the first comes from the Boltzmann factor Eq. (1) and the second from the rate of flux change through the pickup loop Eq. (5).

The SQUID could be very well electrically shielded as it is located near the center of the ferrite rod; near the rod center, the external field has been essentially fully sucked into the rod.

Whether the 900h resolution could be obtained in a semi-open system is an engineering question.

V. MATERIAL PROPERTIES REQUIRED FOR NQR DETECTION

So far, I have only considered RDX, which appears to be the most favorable explosive for NQR detection. The following is a list of required properties:

1. High NQR frequency; the Boltzmann factor in Eq. (1) shows that the signal strength is proportional to ω_0 . For direct electrical pickup, there is another factor of ω_0 in the flux time dependence. Thus, a material such as TNT will have roughly a 10 times smaller signal for SQUID pickup, and a 100 times smaller signal for direct electrical pickup.

2. The material must have a (poly)crystalline structure. This rules out detection of large classes of explosives, including dynamite, plastics, rubbers, slurries, liquids etc. Also, the material must be of a reasonably well defined crystal structure, otherwise the NQR signal will be broadened significantly due to the varying precession frequency. Examples of such effects are local stresses altering the precession frequency within the sample. Although there are echo techniques that allow signal recovery, for the most part, these would be difficult to implement.

3. The NQR precession lifetime must be much longer than the precession period.

In addition, the precession frequency due to the ambient magnetic field must be much less than the NQR frequency; for a 500 mG ambient field, this corresponds to 150 Hz for ^{14}N so this should not be a problem.

VI. CONCLUSIONS

The sensitivity for NQR detection of land-mines is at best marginal; the voltage induced in a pickup coil will be on the order of $0.1 \mu\text{V}$ for 100 g of RDX 20 cm away. This signal scales as the NQR frequency squared for direct electrical detection.

The advantages to the use of a ferrite bar magnetic antenna are described above. The net increase in signal might be as much as a factor of 10.

A SQUID magnetometer might be a possible detection scheme; in this case, the use of a ferrite rod is crucial. Some issues still need to be addressed, such as Barkhausen noise in the ferrite, and Johnson noise (the latter is important for both the direct electrical and SQUID detection methods).

A worrisome aspect of NQR detection is that a null signal does not guarantee the absence of explosives; however, the observation of a signal is absolute evidence for the existence of an explosive. The NQR technic is limited to a small class of explosives, those with a reasonable micro-crystalline structure, and with a large quadrupole precession frequency. It thus appears that NQR might be useful as an auxiliary detection technique within a suite of other measurement devices. Alone, NQR seems to be of rather limited use for explosives detection.

References

1. A. Abragam, *Principles of Nuclear Magnetism* (Oxford, 1989).
2. W.R. Smythe, *Static and Dynamic Electricity* (McGraw-Hill, 1950).